Study of $e^+e^- \to \Lambda\bar{\Lambda}, \Lambda\bar{\Sigma}^0, \Sigma^0\bar{\Sigma}^0$ using initial state radiation with *BABAR*

B. Aubert,[1] M. Bona,[1] D. Boutigny,[1] Y. Karyotakis,[1] J. P. Lees,[1] V. Poireau,[1] X. Prudent,[1] V. Tisserand,[1] A. Zghiche,[1] J. Garra Tico,[2] E. Grauges,[2] L. Lopez,[3] A. Palano,[3] M. Pappagallo,[3] G. Eigen,[4] B. Stugu,[4] L. Sun,[4] G. S. Abrams,[5] M. Battaglia,[5] D. N. Brown,[5] J. Button-Shafer,[5] R. N. Cahn,[5] Y. Groysman,[5] R. G. Jacobsen,[5] J. A. Kadyk,[5] L. T. Kerth,[5] Yu. G. Kolomensky,[5] G. Kukartsev,[5] D. Lopes Pegna,[5] G. Lynch,[5] L. M. Mir,[5] T. J. Orimoto,[5] I. L. Osipenkov,[5] M. T. Ronan,[5,*] K. Tackmann,[5] T. Tanabe,[5] W. A. Wenzel,[5] P. del Amo Sanchez,[6] C. M. Hawkes,[6] A. T. Watson,[6] H. Koch,[7] T. Schroeder,[7] D. Walker,[8] D. J. Asgeirsson,[9] T. Cuhadar-Donszelmann,[9] B. G. Fulsom,[9] C. Hearty,[9] T. S. Mattison,[9] J. A. McKenna,[9] A. Khan,[10] M. Saleem,[10] L. Teodorescu,[10] V. E. Blinov,[11] A. D. Bukin,[11] V. P. Druzhinin,[11] V. B. Golubev,[11] A. P. Onuchin,[11] S. I. Serednyakov,[11] Yu. I. Skovpen,[11] E. P. Solodov,[11] K. Yu. Todyshev,[11] M. Bondioli,[12] S. Curry,[12] I. Eschrich,[12] D. Kirkby,[12] A. J. Lankford,[12] P. Lund,[12] M. Mandelkern,[12] E. C. Martin,[12] D. P. Stoker,[12] S. Abachi,[13] C. Buchanan,[13] S. D. Foulkes,[14] J. W. Gary,[14] F. Liu,[14] O. Long,[14] B. C. Shen,[14] G. M. Vitug,[14] L. Zhang,[14] H. P. Paar,[15] S. Rahatlou,[15] V. Sharma,[15] J. W. Berryhill,[16] C. Campagnari,[16] A. Cunha,[16] B. Dahmes,[16] T. M. Hong,[16] D. Kovalskyi,[16] J. D. Richman,[16] T. W. Beck,[17] A. M. Eisner,[17] C. J. Flacco,[17] C. A. Heusch,[17] J. Kroseberg,[17] W. S. Lockman,[17] T. Schalk,[17] B. A. Schumm,[17] A. Seiden,[17] M. G. Wilson,[17] L. O. Winstrom,[17] E. Chen,[18] C. H. Cheng,[18] F. Fang,[18] D. G. Hitlin,[18] I. Narsky,[18] T. Piatenko,[18] F. C. Porter,[18] R. Andreassen,[19] G. Mancinelli,[19] B. T. Meadows,[19] K. Mishra,[19] M. D. Sokoloff,[19] F. Blanc,[20] P. C. Bloom,[20] S. Chen,[20] W. T. Ford,[20] J. F. Hirschauer,[20] A. Kreisel,[20] M. Nagel,[20] U. Nauenberg,[20] A. Olivas,[20] J. G. Smith,[20] K. A. Ulmer,[20] S. R. Wagner,[20] J. Zhang,[20] A. M. Gabareen,[21] A. Soffer,[21,†] W. H. Toki,[21] R. J. Wilson,[21] F. Winklmeier,[21] D. D. Altenburg,[22] E. Feltresi,[22] A. Hauke,[22] H. Jasper,[22] J. Merkel,[22] A. Petzold,[22] B. Spaan,[22] K. Wacker,[22] V. Klose,[23] M. J. Kobel,[23] H. M. Lacker,[23] W. F. Mader,[23] R. Nogowski,[23] J. Schubert,[23] K. R. Schubert,[23] R. Schwierz,[23] J. E. Sundermann,[23] A. Volk,[23] D. Bernard,[24] G. R. Bonneaud,[24] E. Latour,[24] V. Lombardo,[24] Ch. Thiebaux,[24] M. Verderi,[24] P. J. Clark,[25] W. Gradl,[25] F. Muheim,[25] S. Playfer,[25] A. I. Robertson,[25] J. E. Watson,[25] Y. Xie,[25] M. Andreotti,[26] D. Bettoni,[26] C. Bozzi,[26] R. Calabrese,[26] A. Cecchi,[26] G. Cibinetto,[26] P. Franchini,[26] E. Luppi,[26] M. Negrini,[26] A. Petrella,[26] L. Piemontese,[26] E. Prencipe,[26] V. Santoro,[26] F. Anulli,[27] R. Baldini-Ferroli,[27] A. Calcaterra,[27] R. de Sangro,[27] G. Finocchiaro,[27] S. Pacetti,[27] P. Patteri,[27] I. M. Peruzzi,[27,‡] M. Piccolo,[27] M. Rama,[27] A. Zallo,[27] A. Buzzo,[28] R. Contri,[28] M. Lo Vetere,[28] M. M. Macri,[28] M. R. Monge,[28] S. Passaggio,[28] C. Patrignani,[28] E. Robutti,[28] A. Santroni,[28] S. Tosi,[28] R. S. Dubitzky,[30] J. Marks,[30] S. Schenk,[30] U. Uwer,[30] R. S. Dubitzky,[30] J. Marks,[30] S. Schenk,[30] U. Uwer,[30] D. J. Bard,[31] P. D. Dauncey,[31] R. L. Flack,[31] J. A. Nash,[31] W. Panduro Vazquez,[31] M. Tibbetts,[31] P. K. Behera,[32] X. Chai,[32] M. J. Charles,[32] U. Mallik,[32] J. Cochran,[33] H. B. Crawley,[33] L. Dong,[33] V. Eyges,[33] W. T. Meyer,[33] S. Prell,[33] E. I. Rosenberg,[33] A. E. Rubin,[33] Y. Y. Gao,[34] A. V. Gritsan,[34] Z. J. Guo,[34] C. K. Lae,[34] A. G. Denig,[35] M. Fritsch,[35] G. Schott,[35] N. Arnaud,[36] J. Béquilleux,[36] A. D'Orazio,[36] M. Davier,[36] G. Grosdidier,[36] A. Höcker,[36] V. Lepeltier,[36] F. Le Diberder,[36] A. M. Lutz,[36] S. Pruvot,[36] S. Rodier,[36] P. Roudeau,[36] M. H. Schune,[36] J. Serrano,[36] V. Sordini,[36] A. Stocchi,[36] W. F. Wang,[36] G. Wormser,[36] D. J. Lange,[37] D. M. Wright,[37] I. Bingham,[38] C. A. Chavez,[38] J. R. Fry,[38] E. Gabathuler,[38] R. Gamet,[38] D. E. Hutchcroft,[38] D. J. Payne,[38] K. C. Schofield,[38] C. Touramanis,[38] A. J. Bevan,[39] K. A. George,[39] F. Di Lodovico,[39] R. Sacco,[39] G. Cowan,[40] H. U. Flaecher,[40] D. A. Hopkins,[40] S. Paramesvaran,[40] F. Salvatore,[40] A. C. Wren,[40] D. N. Brown,[41] C. L. Davis,[41] J. Allison,[42] D. Bailey,[42] N. R. Barlow,[42] R. J. Barlow,[42] Y. M. Chia,[42] C. L. Edgar,[42] G. D. Lafferty,[42] T. J. West,[42] J. I. Yi,[42] J. Anderson,[43] C. Chen,[43] A. Jawahery,[43] D. A. Roberts,[43] G. Simi,[43] J. M. Tuggle,[43] G. Blaylock,[44] C. Dallapiccola,[44] S. S. Hertzbach,[44] X. Li,[44] T. B. Moore,[44] E. Salvati,[44] S. Saremi,[43] R. Cowan,[45] D. Dujmic,[45] P. H. Fisher,[45] K. Koeneke,[45] G. Sciolla,[45] M. Spitznagel,[45] F. Taylor,[45] R. K. Yamamoto,[45] M. Zhao,[45] Y. Zheng,[45] S. E. Mclachlin,[46,*] P. M. Patel,[46] S. H. Robertson,[46] A. Lazzaro,[47] F. Palombo,[47] J. M. Bauer,[48] L. Cremaldi,[48] V. Eschenburg,[48] R. Godang,[48] R. Kroeger,[48] D. A. Sanders,[48] D. J. Summers,[48] H. W. Zhao,[48] S. Brunet,[49] D. Côté,[49] M. Simard,[49] P. Taras,[49] F. B. Viaud,[49] H. Nicholson,[50] G. De Nardo,[51] F. Fabozzi,[51,§] L. Lista,[51] D. Monorchio,[51] C. Sciacca,[51] M. A. Baak,[52] G. Raven,[52] H. L. Snoek,[52] C. P. Jessop,[53] K. J. Knoepfel,[53] J. M. LoSecco,[53] G. Benelli,[54] L. A. Corwin,[54] K. Honscheid,[54] H. Kagan,[54] R. Kass,[54] J. P. Morris,[53] A. M. Rahimi,[54] J. J. Regensburger,[54] S. J. Sekula,[54] Q. K. Wong,[54] N. L. Blount,[55] J. Brau,[55] R. Frey,[55] O. Igonkina,[55] J. A. Kolb,[55] M. Lu,[55] R. Rahmat,[55] N. B. Sinev,[55] D. Strom,[55] J. Strube,[55] E. Torrence,[55] N. Gagliardi,[56] A. Gaz,[56] M. Margoni,[56] M. Morandin,[56] A. Pompili,[56] M. Posocco,[56] M. Rotondo,[56] F. Simonetto,[56] R. Stroili,[56] C. Voci,[56] E. Ben-Haim,[57] H. Briand,[57] G. Calderini,[57] J. Chauveau,[57] P. David,[57] L. Del Buono,[57] Ch. de la Vaissière,[57] O. Hamon,[57] Ph. Leruste,[57] J. Malclès,[57] J. Ocariz,[57] A. Perez,[57] J. Prendki,[57] L. Gladney,[58] M. Biasini,[59] R. Covarelli,[59] E. Manoni,[59] C. Angelini,[60] G. Batignani,[60] S. Bettarini,[60] M. Carpinelli,[60] R. Cenci,[60] A. Cervelli,[60] F. Forti,[60] M. A. Giorgi,[60] A. Lusiani,[60] G. Marchiori,[60]

M. A. Mazur,[60] M. Morganti,[60] N. Neri,[60] E. Paoloni,[60] G. Rizzo,[60] J. J. Walsh,[60] J. Biesiada,[61] P. Elmer,[61] Y. P. Lau,[61]
C. Lu,[61] J. Olsen,[61] A. J. S. Smith,[61] A. V. Telnov,[61] E. Baracchini,[62] F. Bellini,[62] G. Cavoto,[62] D. del Re,[62] E. Di Marco,[62]
R. Faccini,[62] F. Ferrarotto,[62] F. Ferroni,[62] M. Gaspero,[62] P. D. Jackson,[62] L. Li Gioi,[62] M. A. Mazzoni,[62] S. Morganti,[62]
G. Piredda,[62] F. Polci,[62] F. Renga,[62] C. Voena,[62] M. Ebert,[63] T. Hartmann,[63] H. Schröder,[63] R. Waldi,[63] T. Adye,[64]
G. Castelli,[64] B. Franek,[64] E. O. Olaiya,[64] W. Roethel,[64] F. F. Wilson,[64] S. Emery,[65] M. Escalier,[65] A. Gaidot,[65]
S. F. Ganzhur,[65] G. Hamel de Monchenault,[65] W. Kozanecki,[65] G. Vasseur,[65] Ch. Yèche,[65] M. Zito,[65] X. R. Chen,[66]
H. Liu,[66] W. Park,[66] M. V. Purohit,[66] R. M. White,[66] J. R. Wilson,[66] M. T. Allen,[67] D. Aston,[67] R. Bartoldus,[67] P. Bechtle,[67]
R. Claus,[67] J. P. Coleman,[67] M. R. Convery,[67] J. C. Dingfelder,[67] J. Dorfan,[67] G. P. Dubois-Felsmann,[67] W. Dunwoodie,[67]
R. C. Field,[67] T. Glanzman,[67] S. J. Gowdy,[67] M. T. Graham,[67] P. Grenier,[67] C. Hast,[67] W. R. Innes,[67] J. Kaminski,[67]
M. H. Kelsey,[67] H. Kim,[67] P. Kim,[67] M. L. Kocian,[67] D. W. G. S. Leith,[67] S. Li,[67] S. Luitz,[67] V. Luth,[67] H. L. Lynch,[67]
D. B. MacFarlane,[67] H. Marsiske,[67] R. Messner,[67] D. R. Muller,[67] C. P. O'Grady,[67] I. Ofte,[67] A. Perazzo,[67] M. Perl,[67]
T. Pulliam,[67] B. N. Ratcliff,[67] A. Roodman,[67] A. A. Salnikov,[67] R. H. Schindler,[67] J. Schwiening,[67] A. Snyder,[67] D. Su,[67]
M. K. Sullivan,[67] K. Suzuki,[67] S. K. Swain,[67] J. M. Thompson,[67] J. Va'vra,[67] A. P. Wagner,[67] M. Weaver,[67]
W. J. Wisniewski,[67] M. Wittgen,[67] D. H. Wright,[67] A. K. Yarritu,[67] K. Yi,[67] C. C. Young,[67] V. Ziegler,[67] P. R. Burchat,[68]
A. J. Edwards,[68] S. A. Majewski,[68] T. S. Miyashita,[68] B. A. Petersen,[68] L. Wilden,[68] S. Ahmed,[69] M. S. Alam,[69] R. Bula,[69]
J. A. Ernst,[69] V. Jain,[69] B. Pan,[69] M. A. Saeed,[69] F. R. Wappler,[69] S. B. Zain,[69] M. Krishnamurthy,[70] S. M. Spanier,[70]
R. Eckmann,[71] J. L. Ritchie,[71] A. M. Ruland,[71] C. J. Schilling,[71] R. F. Schwitters,[71] J. M. Izen,[72] X. C. Lou,[72] S. Ye,[72]
F. Bianchi,[73] F. Gallo,[73] D. Gamba,[73] M. Pelliccioni,[73] M. Bomben,[74] L. Bosisio,[74] C. Cartaro,[74] F. Cossutti,[74]
G. Della Ricca,[74] L. Lanceri,[74] L. Vitale,[74] M. Bomben,[74] L. Bosisio,[74] C. Cartaro,[74] F. Cossutti,[74] G. Della Ricca,[74]
L. Lanceri,[74] L. Vitale,[74] V. Azzolini,[75] N. Lopez-March,[75] F. Martinez-Vidal,[75,‖] D. A. Milanes,[75] A. Oyanguren,[75]
J. Albert,[76] Sw. Banerjee,[76] B. Bhuyan,[76] K. Hamano,[76] R. Kowalewski,[76] I. M. Nugent,[76] J. M. Roney,[76] R. J. Sobie,[76]
P. F. Harrison,[77] J. Ilic,[77] T. E. Latham,[77] G. B. Mohanty,[77] H. R. Band,[78] X. Chen,[78] S. Dasu,[78] K. T. Flood,[78] J. J. Hollar,[78]
P. E. Kutter,[78] Y. Pan,[78] M. Pierini,[78] R. Prepost,[78] S. L. Wu,[78] and H. Neal[79]

(*BABAR* Collaboration)

[1]*Laboratoire de Physique des Particules, IN2P3/CNRS et Université de Savoie, F-74941 Annecy-Le-Vieux, France*
[2]*Universitat de Barcelona, Facultat de Fisica, Departament ECM, E-08028 Barcelona, Spain*
[3]*Università di Bari, Dipartimento di Fisica and INFN, I-70126 Bari, Italy*
[4]*University of Bergen, Institute of Physics, N-5007 Bergen, Norway*
[5]*Lawrence Berkeley National Laboratory and University of California, Berkeley, California 94720, USA*
[6]*University of Birmingham, Birmingham, B15 2TT, United Kingdom*
[7]*Ruhr Universität Bochum, Institut für Experimentalphysik 1, D-44780 Bochum, Germany*
[8]*University of Bristol, Bristol BS8 1TL, United Kingdom*
[9]*University of British Columbia, Vancouver, British Columbia, Canada V6T 1Z1*
[10]*Brunel University, Uxbridge, Middlesex UB8 3PH, United Kingdom*
[11]*Budker Institute of Nuclear Physics, Novosibirsk 630090, Russia*
[12]*University of California at Irvine, Irvine, California 92697, USA*
[13]*University of California at Los Angeles, Los Angeles, California 90024, USA*
[14]*University of California at Riverside, Riverside, California 92521, USA*
[15]*University of California at San Diego, La Jolla, California 92093, USA*
[16]*University of California at Santa Barbara, Santa Barbara, California 93106, USA*
[17]*University of California at Santa Cruz, Institute for Particle Physics, Santa Cruz, California 95064, USA*
[18]*California Institute of Technology, Pasadena, California 91125, USA*
[19]*University of Cincinnati, Cincinnati, Ohio 45221, USA*
[20]*University of Colorado, Boulder, Colorado 80309, USA*
[21]*Colorado State University, Fort Collins, Colorado 80523, USA*
[22]*Universität Dortmund, Institut für Physik, D-44221 Dortmund, Germany*
[23]*Technische Universität Dresden, Institut für Kernund Teilchenphysik, D-01062 Dresden, Germany*
[24]*Laboratoire Leprince-Ringuet, CNRS/IN2P3, Ecole Polytechnique, F-91128 Palaiseau, France*
[25]*University of Edinburgh, Edinburgh EH9 3JZ, United Kingdom*
[26]*Università di Ferrara, Dipartimento di Fisica and INFN, I-44100 Ferrara, Italy*
[27]*Laboratori Nazionali di Frascati dell'INFN, I-00044 Frascati, Italy*
[28]*Università di Genova, Dipartimento di Fisica and INFN, I-16146 Genova, Italy*
[29]*Harvard University, Cambridge, Massachusetts 02138, USA*
[30]*Universität Heidelberg, Physikalisches Institut, Philosophenweg 12, D-69120 Heidelberg, Germany*

[31]Imperial College London, London, SW7 2AZ, United Kingdom

[32]University of Iowa, Iowa City, Iowa 52242, USA

[33]Iowa State University, Ames, Iowa 50011-3160, USA

[34]Johns Hopkins University, Baltimore, Maryland 21218, USA

[35]Universität Karlsruhe, Institut für Experimentelle Kernphysik, D-76021 Karlsruhe, Germany

[36]Laboratoire de l'Accélérateur Linéaire, IN2P3/CNRS et Université Paris-Sud 11, Centre Scientifique d'Orsay, B. P. 34, F-91898 ORSAY Cedex, France

[37]Lawrence Livermore National Laboratory, Livermore, California 94550, USA

[38]University of Liverpool, Liverpool L69 7ZE, United Kingdom

[39]Queen Mary, University of London, E1 4NS, United Kingdom

[40]University of London, Royal Holloway and Bedford New College, Egham, Surrey TW20 0EX, United Kingdom

[41]University of Louisville, Louisville, Kentucky 40292, USA

[42]University of Manchester, Manchester M13 9PL, United Kingdom

[43]University of Maryland, College Park, Maryland 20742, USA

[44]University of Massachusetts, Amherst, Massachusetts 01003, USA

[45]Massachusetts Institute of Technology, Laboratory for Nuclear Science, Cambridge, Massachusetts 02139, USA

[46]McGill University, Montréal, Québec, Canada H3A 2T8

[47]Università di Milano, Dipartimento di Fisica and INFN, I-20133 Milano, Italy

[48]University of Mississippi, University, Mississippi 38677, USA

[49]Université de Montréal, Physique des Particules, Montréal, Québec, Canada H3C 3J7

[50]Mount Holyoke College, South Hadley, Massachusetts 01075, USA

[51]Università di Napoli Federico II, Dipartimento di Scienze Fisiche and INFN, I-80126, Napoli, Italy

[52]NIKHEF, National Institute for Nuclear Physics and High Energy Physics, NL-1009 DB Amsterdam, The Netherlands

[53]University of Notre Dame, Notre Dame, Indiana 46556, USA

[54]Ohio State University, Columbus, Ohio 43210, USA

[55]University of Oregon, Eugene, Oregon 97403, USA

[56]Università di Padova, Dipartimento di Fisica and INFN, I-35131 Padova, Italy

[57]Laboratoire de Physique Nucléaire et de Hautes Energies, IN2P3/CNRS, Université Pierre et Marie Curie-Paris6, Université Denis Diderot-Paris7, F-75252 Paris, France

[58]University of Pennsylvania, Philadelphia, Pennsylvania 19104, USA

[59]Università di Perugia, Dipartimento di Fisica and INFN, I-06100 Perugia, Italy

[60]Università di Pisa, Dipartimento di Fisica, Scuola Normale Superiore and INFN, I-56127 Pisa, Italy

[61]Princeton University, Princeton, New Jersey 08544, USA

[62]Università di Roma La Sapienza, Dipartimento di Fisica and INFN, I-00185 Roma, Italy

[63]Universität Rostock, D-18051 Rostock, Germany

[64]Rutherford Appleton Laboratory, Chilton, Didcot, Oxon, OX11 0QX, United Kingdom

[65]DSM/Dapnia, CEA/Saclay, F-91191 Gif-sur-Yvette, France

[66]University of South Carolina, Columbia, South Carolina 29208, USA

[67]Stanford Linear Accelerator Center, Stanford, California 94309, USA

[68]Stanford University, Stanford, California 94305-4060, USA

[69]State University of New York, Albany, New York 12222, USA

[70]University of Tennessee, Knoxville, Tennessee 37996, USA

[71]University of Texas at Austin, Austin, Texas 78712, USA

[72]University of Texas at Dallas, Richardson, Texas 75083, USA

[73]Università di Torino, Dipartimento di Fisica Sperimentale and INFN, I-10125 Torino, Italy

[74]Università di Trieste, Dipartimento di Fisica and INFN, I-34127 Trieste, Italy

[75]IFIC, Universitat de Valencia-CSIC, E-46071 Valencia, Spain

[76]University of Victoria, Victoria, British Columbia, Canada V8W 3P6

[77]Department of Physics, University of Warwick, Coventry CV4 7AL, United Kingdom

[78]University of Wisconsin, Madison, Wisconsin 53706, USA

[79]Yale University, New Haven, Connecticut 06511, USA

[*]Deceased.

[†]Now at Tel Aviv University, Tel Aviv, 69978, Israel.

[‡]Also with Università di Perugia, Dipartimento di Fisica, Perugia, Italy.

[§]Also with Università della Basilicata, Potenza, Italy.

[‖]Also with Universitat de Barcelona, Facultat de Fisica, Departament ECM, E-08028 Barcelona, Spain.

We study the $e^+e^- \rightarrow \Lambda\bar{\Lambda}\gamma, \Lambda\bar{\Sigma}^0\gamma, \Sigma^0\bar{\Sigma}^0\gamma$ processes using 230 fb^{-1} of integrated luminosity collected by the *BABAR* detector at e^+e^- center-of-mass energy of 10.58 GeV. From the analysis of the baryon-antibaryon mass spectra the cross sections for $e^+e^- \rightarrow \Lambda\bar{\Lambda}, \Lambda\bar{\Sigma}^0, \Sigma^0\bar{\Sigma}^0$ are measured in the dibaryon mass range from threshold up to 3 GeV/c^2. The ratio of electric and magnetic form factors, $|G_E/G_M|$, is measured for $e^+e^- \rightarrow \Lambda\bar{\Lambda}$, and limits on the relative phase between Λ form factors are obtained. We also measure the $J/\psi \rightarrow \Lambda\bar{\Lambda}, \Sigma^0\bar{\Sigma}^0$, and $\psi(2S) \rightarrow \Lambda\bar{\Lambda}$ branching fractions.

I. INTRODUCTION

In this paper we continue the experimental study of baryon timelike electromagnetic form factors. In our previous work [1] we have measured the energy dependence of the cross section for $e^+e^- \rightarrow p\bar{p}$ and of the proton form factor using the initial state radiation (ISR) technique. Here we use this technique to study the processes [1] $e^+e^- \rightarrow \Lambda\bar{\Lambda}$, $\Sigma^0\bar{\Sigma}^0, \Lambda\bar{\Sigma}^0$. The Born cross section for the ISR process $e^+e^- \rightarrow f + \gamma$ (Fig. 1), where f is a hadronic system, integrated over the hadron momenta, is given by

$$\frac{d\sigma_{e^+e^- \rightarrow f\gamma}(m)}{dm \, d\cos\theta_\gamma^*} = \frac{2m}{s} W(x, \theta_\gamma^*)\sigma_f(m), \qquad (1)$$

where $\sqrt{s}$ is the e^+e^- center-of-mass energy (c.m.), m is the invariant mass of the hadronic system, $\sigma_f(m)$ is the cross section for $e^+e^- \rightarrow f$ reaction, $x \equiv E_\gamma^*/\sqrt{s} = 1 - m^2/s$, and E_γ^* and θ_γ^* are the ISR photon energy and polar angle, respectively, in the e^+e^- c.m. frame.[2] The function [2]

$$W(x, \theta_\gamma^*) = \frac{\alpha}{\pi x}\left(\frac{2 - 2x + x^2}{\sin^2\theta_\gamma^*} - \frac{x^2}{2}\right) \qquad (2)$$

describes the probability of ISR photon emission for $\theta_\gamma^* \gg m_e/\sqrt{s}$, where α is the fine structure constant and m_e is the electron mass.

The cross section for the process $e^+e^- \rightarrow B\bar{B}$, where B is a spin-1/2 baryon, depends on magnetic (G_M) and electric (G_E) form factors as follows:

$$\sigma_{B\bar{B}}(m) = \frac{4\pi\alpha^2\beta}{3m^2}\left[|G_M(m)|^2 + \frac{1}{2\tau}|G_E(m)|^2\right], \qquad (3)$$

where $\beta = \sqrt{1 - 4m_B^2/m^2}$ and $\tau = m^2/4m_B^2$; at threshold, $G_E = G_M$. The cross section determines the linear combination of the squared form factors

$$|F(m)|^2 = \frac{2\tau|G_M(m)|^2 + |G_E(m)|^2}{2\tau + 1}, \qquad (4)$$

and we define $|F(m)|$ to be the effective form factor [1].

---

[1]Throughout this paper the use of charge conjugate modes is implied.

[2]Throughout this paper the asterisk denotes quantities in the e^+e^- c.m. frame.

The modulus of the ratio of electric and magnetic form factors can be determined from the analysis of the distribution of $\cos\theta_B$, where θ_B is the angle between the baryon momentum in the dibaryon rest frame and the momentum of the $B\bar{B}$ system in the e^+e^- c.m. frame. This distribution can be expressed as the sum of the terms proportional to $|G_M|^2$ and $|G_E|^2$. The θ_B dependencies of the G_E and G_M terms are close to $\sin^2\theta_B$ and $1 + \cos^2\theta_B$ angular distributions for electric and magnetic form factors in the $e^+e^- \rightarrow B\bar{B}$ process. The full differential cross section for $e^+e^- \rightarrow B\bar{B}\gamma$ [3] is given in the Appendix.

A nonzero relative phase between the electric and magnetic form factors manifests itself in polarization of the outgoing baryons. In the $e^+e^- \rightarrow B\bar{B}$ reaction this polarization is perpendicular to the production plane [4]. For the ISR process $e^+e^- \rightarrow B\bar{B}\gamma$ the polarization observables are analyzed in Refs. [3,5]. The expression for the baryon polarization as a function of G_E, G_M, and momenta of the initial electron, ISR photon, and final baryon [3] is given in the Appendix. In the case of the $\Lambda\bar{\Lambda}$ final state the $\Lambda \rightarrow p\pi^-$ decay can be used to measure the Λ polarization and hence the phase between the form factors.

Experimental information on the $e^+e^- \rightarrow \Lambda\bar{\Lambda}, \Sigma^0\bar{\Sigma}^0$, $\Lambda\bar{\Sigma}^0$ reactions is very scarce. The $e^+e^- \rightarrow \Lambda\bar{\Lambda}$ cross section is measured as 100^{+65}_{-35} pb at 2.386 GeV, and at the same energy upper limits for $e^+e^- \rightarrow \Sigma^0\bar{\Sigma}^0$ (< 120 pb) and $e^+e^- \rightarrow \Lambda\bar{\Sigma}^0$ (< 75 pb) cross sections have been obtained [6]. No other experimental results exist.

II. THE *BABAR* DETECTOR AND DATA SAMPLES

We analyze a data sample corresponding to an integrated luminosity of 230 fb^{-1} recorded with the *BABAR* detector [7] at the PEP-II asymmetric-energy storage rings. At PEP-II, 9-GeV electrons collide with 3.1-GeV positrons at a center-of-mass energy of 10.58 GeV [the Υ (4S) reso-
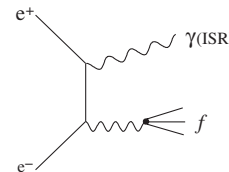

FIG. 1. The Feynman diagram describing the ISR process $e^+e^- \rightarrow f\gamma$, where f is a hadronic system.

nance]. Additional data ($\sim 10\%$) recorded at 10.54 GeV are included in the present analysis.

Charged-particle tracking is provided by a five-layer silicon vertex tracker (SVT) and a 40-layer drift chamber (DCH), operating in a 1.5-T axial magnetic field. The transverse momentum resolution is 0.47% at 1 GeV/c. Energies of photons and electrons are measured with a CsI(Tl) electromagnetic calorimeter (EMC) with a resolution of 3% at 1 GeV. Charged-particle identification is provided by specific ionization (dE/dx) measurements in the SVT and DCH, and by an internally reflecting ring-imaging Cherenkov detector (DIRC). Muons are identified in the solenoid's instrumented flux return, which consists of iron plates interleaved with resistive plate chambers.

Signal ISR processes are simulated with the Monte Carlo (MC) event generator Phokhara [8,9]. Because the polar-angle distribution of the ISR photon is peaked near 0° and 180°, the MC events are generated with a restriction on the photon polar angle: $20° < \theta_\gamma^* < 160°$. The Phokhara event generator includes next-to-leading-order radiative corrections to the Born cross section. In particular, it generates an extra soft photon emitted from the initial state. To restrict the maximum energy of the extra photon we require that the invariant mass of the dibaryon system and the ISR photon satisfies $M_{B\bar{B}\gamma} > 8$ GeV/c^2. The generated events are subjected to detailed detector simulation based on GEANT4 [10], and are reconstructed with the software chain used for the experimental data. Variations in the detector and in the beam background conditions are taken into account. For the full simulation we use the differential cross section for the $e^+e^- \to B\bar{B}\gamma$ process with $G_E = G_M$. In order to study angular distributions and model dependence of detection efficiency, we produce two large samples of simulated events at the generator level, one with $G_E = 0$ and the other with $G_M = 0$, and reweight the events from the full simulation sample according to the desired $|G_E/G_M|$ ratio.

Background from $e^+e^- \to q\bar{q}$, where q represents a u, d, s, or c quark, is simulated with the JETSET [11] event

generator. JETSET also generates ISR events with hadron invariant mass above 2 GeV/c^2 and therefore can be used to study ISR background with baryons in the final state. The most important background processes, $e^+e^- \to B\bar{B}\pi^0\gamma$, $e^+e^- \to B\bar{B}\pi^0$, and $e^+e^- \to \Lambda\bar{p}K^+\gamma$, are simulated separately. Three-body phase space and the Bonneau-Martin formula [2] are used to generate the angular and energy distributions for the final hadrons and ISR photon, respectively. For these processes extra soft-photon radiation from the initial state is generated using the structure function method [12].

III. THE REACTION $e^+e^- \to \Lambda\bar{\Lambda}\gamma$

A. Event selection

The initial selection of events requires the presence of a high energy photon and at least one Λ and one $\bar{\Lambda}$ candidate. The hard photon must have energy in the c.m. frame $E_\gamma^* > 3$ GeV. The $\Lambda \to p\pi^-$ decay mode with the branching fraction of $(63.9 \pm 0.5)\%$ [13] is used to identify Λ candidates. Two oppositely charged tracks are assigned the proton and pion mass hypotheses and fitted to a common vertex. Any combination with invariant mass in the range 1.104–1.128 GeV/c^2 [the nominal Λ mass is 1.115683(6) GeV/c^2 [13]], laboratory momentum greater than 0.5 GeV/c, and fit probability greater than 0.001 is considered a Λ candidate. The candidate is then refitted with a Λ mass constraint to improve the precision of the Λ momentum measurement. To suppress combinatorial background we require that at least one of the proton candidates be identified as a proton according to the specific ionization (dE/dx) measured in the SVT and DCH, and the Cherenkov angle measured in the DIRC.

For events passing the preliminary selection, we perform a kinematic fit that imposes energy and momentum conservation at the production vertex to the Λ and $\bar{\Lambda}$ candidates and the photon with highest E_γ^*. For events with more than one Λ ($\bar{\Lambda}$) candidate we consider all possible $\Lambda\bar{\Lambda}$ combinations, and the one giving the lowest χ^2 for the
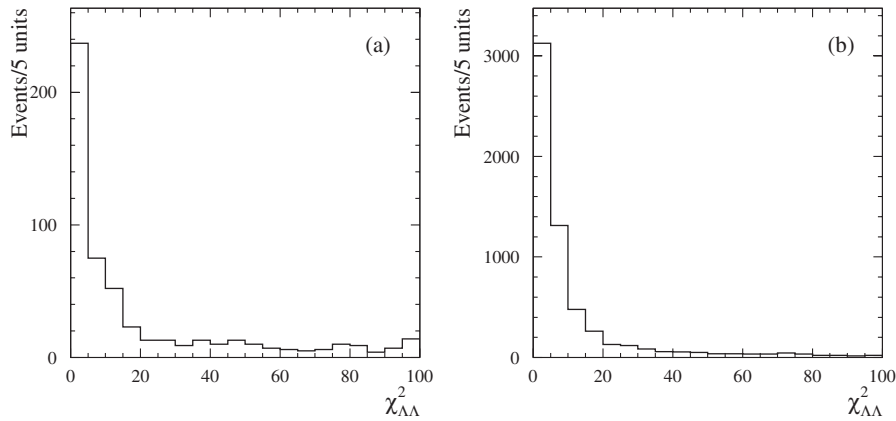

FIG. 2. The $\chi^2_{\Lambda\Lambda}$ distributions for data (a) and $e^+e^- \to \Lambda\bar{\Lambda}\gamma$ simulation (b).
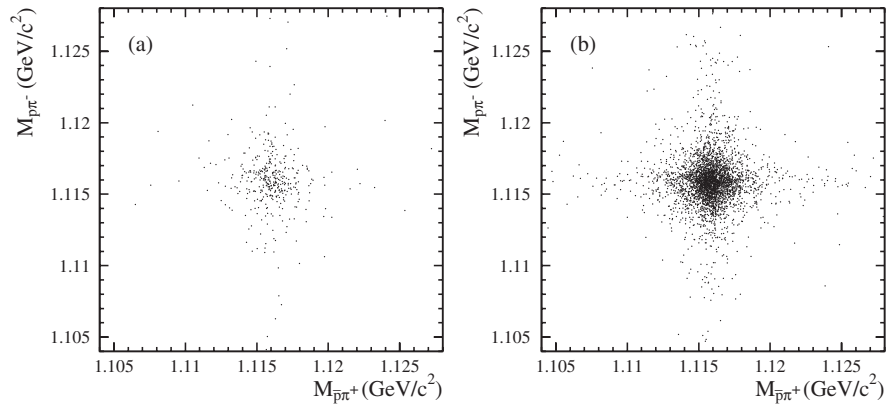
FIG. 3.   Scatter plots of the invariant mass of the Λ candidate versus the invariant mass of the $\bar{\Lambda}$ candidate for data (a) and $e^+e^- \rightarrow \Lambda\bar{\Lambda}\gamma$ simulation (b).

kinematic fit is retained. The MC simulation does not accurately reproduce the shape of the resolution function for the photon energy. This leads to a difference in the χ^2 distributions resulting from the kinematic fits to data and simulated events. To reduce this difference, only the measured direction of the ISR photon is used in the fit; its energy is a fit parameter.

The χ^2 distributions for the kinematic fit ($\chi^2_{\Lambda\Lambda}$) to data events and to simulated $e^+e^- \rightarrow \Lambda\bar{\Lambda}\gamma$ events are shown in Fig. 2. We select the events with $\chi^2_{\Lambda\Lambda} < 20$ for further analysis. The control region $20 < \chi^2_{\Lambda\Lambda} < 40$ is used for background estimation and subtraction.

Possible sources of background for the process under study are those with only one Λ in the final state, such as $e^+e^- \rightarrow \Lambda\bar{p}K^+\gamma$. Such events contain a charged kaon instead of one of the pion candidates. To suppress this background we require that no charged pion candidate be identified as a kaon. This requirement rejects 70% of the

FIG. 4.   The $\Lambda\bar{\Lambda}$ mass spectrum for events satisfying the $\Lambda\bar{\Lambda}\gamma$ selection criteria.

background from $e^+e^- \rightarrow \Lambda\bar{p}K^+\gamma$ and only ~2% of signal events.

The scatter plot of the invariant mass of the Λ candidate versus the invariant mass of the $\bar{\Lambda}$ candidate for the 387 data events passing all the selection criteria is shown in Fig. 3(a) and that for simulated $e^+e^- \rightarrow \Lambda\bar{\Lambda}\gamma$ events is shown in Fig. 3(b). The $\Lambda\bar{\Lambda}$ invariant mass spectrum for data events is shown in Fig. 4. About half of the events have invariant mass below 3 GeV/c^2. Signals due to $J/\psi \rightarrow \Lambda\bar{\Lambda}$ and $\psi(2S) \rightarrow \Lambda\bar{\Lambda}$ decays are also clearly seen.

B. Background subtraction

Processes of three kinds potentially contribute background to the $e^+e^- \rightarrow \Lambda\bar{\Lambda}\gamma$ data sample, namely, those with zero, one, and two Λ's in the final state.

The composition of the one-Λ background is studied using JETSET simulation. This background is dominated by $e^+e^- \rightarrow \Lambda\bar{p}K^+\gamma$ events. Other processes also contain a charged kaon in the final state. The level of the one-Λ background can be estimated from the fraction of data events rejected by the requirement that no π^+ candidate be identified as a K^+. For $M_{\Lambda\bar{\Lambda}} < 3$ GeV/c^2 this fraction is 3/224, and we estimate that the one-Λ background does not exceed 1.6 events at 90% confidence level (CL).

A more precise estimation (but based on the JETSET prediction for the composition of one-Λ events) of this background is obtained using a special selection of $e^+e^- \rightarrow \Lambda\bar{p}K^+\gamma$ events. We select events with at least four charged tracks and a photon with $E^*_\gamma > 3$ GeV. Two tracks, one of which is identified as a proton, must be combined to form a Λ candidate, and the other two must originate from the e^+e^- interaction point and be identified as an antiproton and a positively charged kaon. For these events we perform the kinematic fit to the $e^+e^- \rightarrow \Lambda\bar{p}K^+\gamma$ hypothesis and require $\chi^2 < 20$. The background for $e^+e^- \rightarrow \Lambda\bar{p}K^+\gamma$ is estimated from the region $20 < \chi^2 < 40$. The total number of selected $\Lambda\bar{p}K^+\gamma$ events is found to be 568 ± 30. Using the ratio of detection efficien-
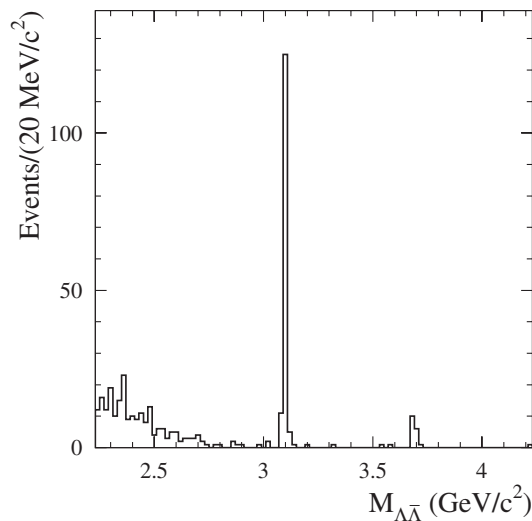
cies for $\Lambda\bar{\Lambda}\gamma$ and $\Lambda\bar{p}K^+\gamma$ selections obtained from simulation, $(0.12 \pm 0.07)\%$, we calculate the number of $\Lambda\bar{p}K^+\gamma$ events satisfying the $\Lambda\bar{\Lambda}\gamma$ selection criteria to be 0.7 ± 0.4. Taking the ratio of $\Lambda\bar{p}K^+\gamma$ to all one-Λ events (0.7) from JETSET simulation, we estimate the total number of one-Λ background events to be 1.0 ± 0.6. The $e^+e^- \to \Lambda\bar{p}K^+\gamma$ simulation is reweighted to reproduce the shape of the experimental $M_{\Lambda pK}$ distribution. The reweighted events are then used to find the distribution of $M_{\Lambda\bar{\Lambda}}$ for events with only one real Λ. We estimate 0.8 ± 0.5 background events to have $M_{\Lambda\bar{\Lambda}} < 3$ GeV/c^2.

The background processes with no real Λ's are ISR processes with four charged particles in the final state: $e^+e^- \to 2\pi^+2\pi^-\gamma$, $K^+K^-\pi^+\pi^-\gamma$, $K^+K_S\pi^-\gamma$, $p\bar{p}\pi^+\pi^-\gamma$, $2\pi^+2\pi^-\pi^0$, etc. The background from these processes can be estimated from an analysis of the two-dimensional distribution of the Λ and $\bar{\Lambda}$ candidate mass values. The 6×6 two-dimensional histogram corresponding to the plot in Fig. 3(a) is fitted by the following function:

$$n_{ij} = N_2 S_i S_j + N_0 B_{0i}B_{0j} + N_1(S_i B_{1j} + S_j B_{1i})/2, \quad (5)$$

where the six mass intervals are those shown in Fig. 5. Here N_2, N_1, and N_0 represent the numbers of events with two, one, and zero Λ's, respectively; N_2 and N_0 are free fit parameters, and N_1 is fixed at the value determined above (0.8 ± 0.5 events for $M_{\Lambda\bar{\Lambda}} < 3$ GeV/c^2); S_i is the probability for a Λ to have reconstructed mass in the ith mass bin, while B_{0i} and B_{1i} are the probabilities for a false Λ candidate from background with zero and one real Λ, respectively. Since the one-Λ background is small and its presence leads to only small changes in the fitted N_2 and N_0 values, we use a uniform distribution for $B_1(m)$, i.e. all $B_{1i} = 1/6$. The $B_0(m)$ are parametrized by the linear function $B_{0i} = 1/6 + (i - 3.5)\Delta$, and five of the S_i and Δ are free fit parameters. For 221 events with $M_{\Lambda\bar{\Lambda}} < 3$ GeV/c^2

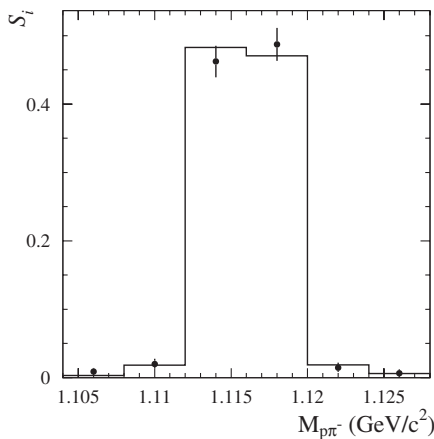
FIG. 5. The values of S_i (see text) obtained from fits to data (points with error bars) and from fits to $e^+e^- \to \Lambda\bar{\Lambda}\gamma$ simulated events (histogram).

the fit yields $N_2 = 216 \pm 15$ and $N_0 = 4^{+4}_{-3}$. The fitted values of the S_i are in good agreement with the values expected from $e^+e^- \to \Lambda\bar{\Lambda}\gamma$ simulation (Fig. 5). In particular, $S_3 + S_4 = 0.950 \pm 0.014$ for data and 0.953 ± 0.003 for simulation.

The sources of two-Λ background are processes with an extra neutral particle(s) in the final state: $e^+e^- \to \Lambda\bar{\Lambda}\pi^0$, $e^+e^- \to \Lambda\bar{\Lambda}\gamma\gamma$, $e^+e^- \to \Lambda\bar{\Lambda}\pi^0\gamma$, etc. A significant fraction of $e^+e^- \to \Lambda\bar{\Lambda}\pi^0$ events with an undetected low-energy photon or with merged photons from π^0 decay are reconstructed under the $\Lambda\bar{\Lambda}\gamma$ hypothesis with a low value of $\chi^2_{\Lambda\bar{\Lambda}}$, and cannot be separated from the process under study. This background is studied by selecting a special subsample of events containing a Λ and a $\bar{\Lambda}$ candidate and at least two photons, one with energy greater than 0.1 GeV and the other with c.m. energy above 3 GeV. The two-photon invariant mass is required to be in the range 0.07 to 0.2 GeV/c^2. A kinematic fit to the $e^+e^- \to \Lambda\bar{\Lambda}\gamma\gamma$ hypothesis is then performed. Requirements on the χ^2 ($\chi^2 < 20$) and the two-photon invariant mass ($0.11 < M_{\gamma\gamma} < 0.16$ GeV/c^2) are imposed to define $\Lambda\bar{\Lambda}\pi^0$ candidates. No data events satisfy these criteria, and the expected background from $e^+e^- \to \Lambda\bar{\Lambda}\gamma$ is 0.8 ± 0.3 events. The corresponding 90% CL upper limit on the number of selected $\Lambda\bar{\Lambda}\pi^0$ candidates is 1.6 events. Using the ratio of detection efficiencies for $\Lambda\bar{\Lambda}\pi^0$ and $\Lambda\bar{\Lambda}\gamma$ selections (0.28 ± 0.02) we find that the $\Lambda\bar{\Lambda}\pi^0$ background in the $\Lambda\bar{\Lambda}\gamma$ sample does not exceed six events. This upper limit is used as a measure of the systematic uncertainty due to $\Lambda\bar{\Lambda}\pi^0$ background. We assume that the dibaryon mass spectrum in the $e^+e^- \to \Lambda\bar{\Lambda}\pi^0$ process is similar to that for the $p\bar{p}\pi^0$ final state [1]. In particular, about 70% of $\Lambda\bar{\Lambda}\pi^0$ events are located in the $\Lambda\bar{\Lambda}$ mass region below 3 GeV/c^2. For this mass range this background does not exceed 2% of the selected $\Lambda\bar{\Lambda}\gamma$ candidates.

The two-Λ background other than from $e^+e^- \to \Lambda\bar{\Lambda}\pi^0$ has the $\chi^2_{\Lambda\Lambda}$ distribution very different from that for the process under study. Table I shows the ratio of numbers of selected $\Lambda\bar{\Lambda}\gamma$ candidates with $20 < \chi^2_{\Lambda\Lambda} < 40$ and $\chi^2_{\Lambda\Lambda} < 20$ for signal and background processes. The ratios are obtained from simulation. The column denoted "JETSET" shows the result of JETSET simulation for background events containing two Λ's in the final state. From the number of selected two-Λ events in the signal and control $\chi^2_{\Lambda\Lambda}$ regions, $N_2(\chi^2 < 20)$ and $N_2(20 < \chi^2 < 40)$, the numbers of signal and background events with $\chi^2_{\Lambda\Lambda} < 20$ can be calculated as

$$N_{2s} = \frac{N_2(\chi^2 < 20) - N_2(20 < \chi^2 < 40)/\beta_{bkg}}{1 - \beta_{sig}/\beta_{bkg}}, \quad (6)$$

$$N_{2b} = N_2(\chi^2 < 20) - N_{2s},$$

TABLE I.   The β_i values obtained from simulation for signal and background processes, where β_i is the ratio of the number of selected $\Lambda\bar{\Lambda}\gamma$ candidates with $20 < \chi^2_{\Lambda\Lambda} < 40$ to that with $\chi^2_{\Lambda\Lambda} < 20$.

	$\Lambda\bar{\Lambda}\gamma$	$\Lambda\bar{\Sigma}^0\gamma$	$\Sigma^0\bar{\Sigma}^0\gamma$	$\Lambda\bar{\Sigma}^0\pi^0$	JETSET
β_i	0.073 ± 0.005	0.83 ± 0.07	1.1 ± 0.2	0.81 ± 0.09	0.86 ± 0.06

TABLE II. N is the number of selected $\Lambda\bar{\Lambda}\gamma$ candidates with $M_{\Lambda\bar{\Lambda}} < 3$ GeV/c^2; N_{2s} is the number of signal events; N_0, N_1, N_{2b} indicate the number of background events with zero, one, and two Λ's in the final state, respectively; and $N_{\Lambda\bar{\Lambda}\pi^0}$ is background from $e^+e^- \to \Lambda\bar{\Lambda}\pi^0$.

	N	N_{2s}	N_0	N_1	N_{2b}	$N_{\Lambda\bar{\Lambda}\pi^0}$
$\chi^2_{\Lambda\Lambda} < 20$	221	204 ± 19	4^{+4}_{-3}	0.8 ± 0.5	12 ± 10	<4
$20 < \chi^2_{\Lambda\Lambda} < 40$	35	15 ± 3	9^{+7}_{-5}	0.6 ± 0.4	11 ± 8	<1
$\chi^2_{\Lambda\Lambda} < 20$ (JETSET)	522	500 ± 17	2.5 ± 1.2	0.6 ± 0.6	18 ± 3	1.2 ± 0.9

where β_{bkg} is the ratio of fractions of events in the control and signal χ^2 regions averaged over all processes contributing to two-Λ background. For this coefficient we use $\beta_{\text{bkg}} = 0.9 \pm 0.3$ which is close to the value obtained from the JETSET simulation, with an uncertainty covering the β_i variations for different background processes. For the ratio for the signal process β_{sig}, we use the value obtained from simulation, $\beta_{\text{sig}} = 0.073 \pm 0.010$. The quoted error takes into account MC statistics, the data-MC simulation difference in χ^2 distribution, and the β_{sig} variation as a function of $\Lambda\bar{\Lambda}$ mass. The difference between data and simulated χ^2 distributions was studied in Ref. [1] using the process $e^+e^- \to \mu^+\mu^-\gamma$. The resulting values of N_{2s} and N_{2b} for $\Lambda\bar{\Lambda}$ masses below 3 GeV/c^2 are listed in Table II. The total background in the signal χ^2 region from the processes with zero, one, and two Λ's in final state is about 10%. The last row of the table shows the JETSET prediction for signal and background events in the signal χ^2 region.

The simulation overestimates the signal yield, but can be used for qualitative estimation of background level.

The procedure for background estimation and subtraction described above is applied in each of the 12 $\Lambda\bar{\Lambda}$ mass intervals indicated in Table IV. Because of restricted statistics we fit the two-dimensional histogram of $M_{p\pi^-}$ vs $M_{\bar{p}\pi^+}$ using 3×3 bins, and fix the S_i [see Eq. (5)] at the values obtained from MC simulation. The histograms for signal and control χ^2 regions are fitted simultaneously. The free fit parameters are N_0 and Δ for the two χ^2 regions, N_{2s} and N_{2b}. Figure 6 shows the distribution of selected events over the chosen mass intervals. The shaded histogram shows the background contribution obtained from the fit. The resulting numbers of signal events are listed in Table IV, where the quoted errors include the statistical errors and errors due to uncertainties in the β_{sig}, β_{bkg}, and S_i coefficients. These coefficients are varied within their uncertainties during fitting. For the mass ranges $3.2 < M_{\Lambda\bar{\Lambda}} < 3.6$ GeV/c^2 and $3.8 < M_{\Lambda\bar{\Lambda}} < 5.0$ GeV/c^2 where we do not see evidence for a signal above background, 90% CL upper limits on the number of signal events are listed. The mass regions near the J/ψ and $\psi(2S)$ will be considered separately in Sec. III F.

C. Angular distributions for $e^+e^- \to \Lambda\bar{\Lambda}\gamma$

The modulus of the ratio of the electric and magnetic form factors can be extracted from an analysis of the distribution of $\cos\theta_\Lambda$, where θ_Λ is the angle between the Λ momentum in the $\Lambda\bar{\Lambda}$ rest frame and the momentum of the $\Lambda\bar{\Lambda}$ system in the e^+e^- c.m. frame. This distribution is given by

$$\frac{dN}{d\cos\theta_\Lambda} = A[H_M(\cos\theta_\Lambda, M_{\Lambda\bar{\Lambda}})$$

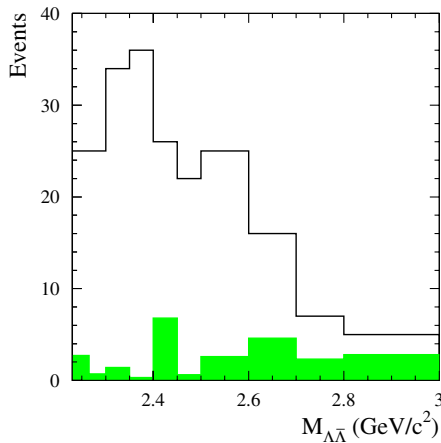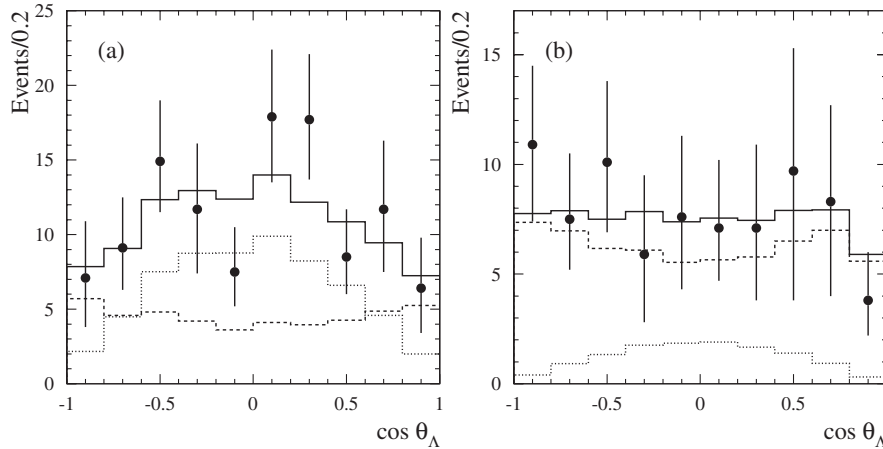$$+ \left|\frac{G_E}{G_M}\right|^2 H_E(\cos\theta_\Lambda, M_{\Lambda\bar{\Lambda}})]. \quad (7)$$

FIG. 6 (color online).   The distribution of data events satisfying the $\Lambda\bar{\Lambda}\gamma$ selection criteria over chosen mass intervals. The shaded histogram shows fitted background.

FIG. 7. The $\cos\theta_\Lambda$ distribution for the mass regions 2.23–2.40 GeV/c^2 (a) and 2.40–2.80 GeV/c^2 (b). The points with error bars represent the data after background subtraction. The histograms are fit results: the dashed histogram shows the contributions corresponding to the magnetic form factor, the dotted histogram shows the contribution from the electric form factor, and the solid histogram is the sum of these two.

The functions $H_M(\cos\theta_\Lambda, M_{\Lambda\bar{\Lambda}})$ and $H_E(\cos\theta_\Lambda, M_{\Lambda\bar{\Lambda}})$ do not have an analytic form, and so are calculated using MC simulation. To do this, two samples of $e^+e^- \to \Lambda\bar{\Lambda}\gamma$ events were generated, one with $G_E = 0$ and the other with $G_M = 0$, using generator level simulation. The angular dependencies of the resulting functions do not differ significantly from the $(1 + \cos^2\theta_\Lambda)$ and $\sin^2\theta_\Lambda$ functions corresponding to the magnetic and electric form factors in the case of $e^+e^- \to \Lambda\bar{\Lambda}$.

The observed angular distributions are fitted in two mass intervals: from $\Lambda\bar{\Lambda}$ threshold to 2.4 GeV/c^2 and from 2.4 GeV/c^2 to 2.8 GeV/c^2. For each mass and angular interval, the background is subtracted by means of the procedure described in the previous section. The angular distributions obtained are shown in Fig. 7.

The distributions are fitted using the expression on the right-hand side of Eq. (7) with two free parameters A and $|G_E/G_M|$. The functions H_M and H_E are replaced by the histograms, obtained from MC simulation with the $\Lambda\bar{\Lambda}$ selection criteria applied. To take into account the effect of these criteria (Fig. 8), the simulated events produced assuming $G_E = G_M$ are reweighted according to the $\cos\theta_\Lambda$ distributions obtained at generator level. These weight functions also take account of the difference in $\Lambda\bar{\Lambda}$ mass dependence between data and MC simulation. The histograms fitted to the angular distributions are shown in Fig. 7. The following values of the $|G_E/G_M|$ ratio are obtained:

$$|G_E/G_M| = 1.73^{+0.99}_{-0.57} \ (2.23\text{–}2.40 \text{ GeV}/c^2),$$

$$|G_E/G_M| = 0.71^{+0.66}_{-0.71} \ (2.40\text{–}2.80 \text{ GeV}/c^2).$$

The quoted errors include both statistical and systematic uncertainties. The net systematic uncertainty does not exceed 15% of the statistical error and includes the un-

certainties due to background subtraction, limited MC statistics, and the mass dependence of the $|G_E/G_M|$ ratio.

We also measure the angular distribution for $J/\psi \to \Lambda\bar{\Lambda}$ decay, for which the shape is usually described by the form $(1 + \alpha\cos^2\theta)$. The world-average value of $\alpha = 0.65 \pm 0.10$ [14–16]. The distribution for $J/\psi \to \Lambda\bar{\Lambda}$ decay in the present experiment is shown in Fig. 9. To remove background, this distribution was obtained as the difference between the histogram for the signal mass region (3.05–3.15 GeV/c^2) and that for the mass sidebands (3.00–3.05 and 3.15–3.20 GeV/c^2). The data distribution is in good agreement with that obtained from simulation with $\alpha = 0.65$.

Our results on the $|G_E/G_M|$ ratio are consistent both with $|G_E/G_M| = 1$, valid at the $\Lambda\bar{\Lambda}$ threshold, and with our results for the reaction $e^+e^- \to p\bar{p}$ for which this ratio was found to be greater than unity near threshold [1]. The
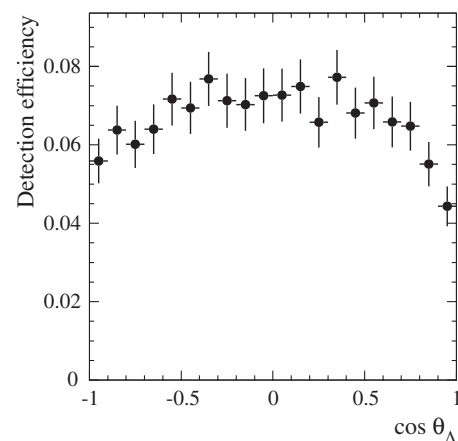

FIG. 8. The $\cos\theta_\Lambda$ dependence of the detection efficiency for simulated events with $M_{\Lambda\bar{\Lambda}} < 2.8$ GeV/c^2.
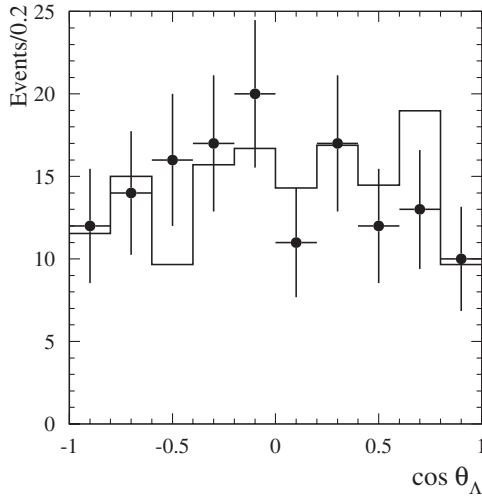
FIG. 9. The $\cos\theta_\Lambda$ distributions for data (points with error bars) and simulation (histogram) corresponding to the reaction $e^+e^- \to J/\psi\gamma \to \Lambda\bar{\Lambda}\gamma$.

strong dependence of the $|G_E/G_M|$ ratio on the dibaryon mass near threshold is expected due to the baryon-antibaryon final state interaction [17,18].

D. Mass dependence of the detection efficiency

To first approximation the detection efficiency is determined from MC simulation as the ratio of true $\Lambda\bar{\Lambda}$ mass distributions computed after and before applying the selection criteria. Since the $e^+e^- \to \Lambda\bar{\Lambda}\gamma$ differential cross section depends on two form factors, the detection efficiency cannot be determined in a model-independent way. We use a model in which the $|G_E/G_M|$ ratio is set to the values obtained from the fits to the experimental angular distributions for $M_{\Lambda\bar{\Lambda}} < 2.8$ GeV/c^2, and then set $|G_E/G_M| = 1$ for higher masses. The detection efficiency obtained in this way is shown in Fig. 10. This
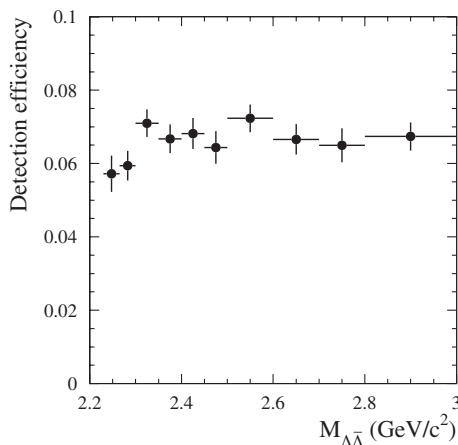

FIG. 10. The $\Lambda\bar{\Lambda}$ mass dependence of detection efficiency obtained from MC simulation.

efficiency includes the branching fraction for $\Lambda \to p\pi^-$ decay, which is $(63.9 \pm 0.5)\%$ [13]. For $M_{\Lambda\bar{\Lambda}} <$ 2.8 GeV/c^2 the variation of the $|G_E/G_M|$ ratio within its experimental uncertainties leads to a 2.5% model uncertainty. For higher masses, the model uncertainty is taken as half the difference between the detection efficiencies corresponding to $G_E = 0$ and $G_M = 0$; this yields a 5% uncertainty.

The efficiency determined from MC simulation (ε_{MC}) must be corrected to account for data-MC simulation differences in detector response:

$$\varepsilon = \varepsilon_{\text{MC}}\prod_i(1 + \delta_i), \qquad (8)$$

where the δ_i's correct for the several effects discussed below and summarized in Table III.

The efficiency correction for the χ^2 requirement was studied in Ref. [1] for $e^+e^- \to \mu^+\mu^-\gamma$ and in Ref. [19] for $e^+e^- \to 2\pi^+2\pi^-\gamma$. The corrections were found to be $-(1.0 \pm 1.3)\%$ and $-(3 \pm 2)\%$, respectively. For $e^+e^- \to \Lambda\bar{\Lambda}\gamma$ we double the correction for $\mu^+\mu^-\gamma$, and assign a systematic uncertainty equal to the correction.

The effect of requiring no identified K is studied using $e^+e^- \to J/\psi\gamma \to \Lambda\bar{\Lambda}\gamma$ events. The number of J/ψ events is determined using the sideband subtraction method. The event losses when requiring no identified K are found to be $(2.1 \pm 1.2)\%$ in data and $(1.1 \pm 0.4)\%$ in MC simulation. The difference of these numbers is taken as the efficiency correction.

Another source of data-MC simulation difference is track loss. The correction due to the difference in track reconstruction is estimated to be -0.25% per track with systematic uncertainty 0.7% for each proton and 1.2% for each pion, which has a softer momentum spectrum. Specifically, for the antiproton track only, an extra systematic error originates from imperfect simulation of nuclear interactions of antiprotons in the detector material. This effect was studied in [1], and the corresponding efficiency correction is found to be $(1.0 \pm 0.4)\%$. All corrections for track reconstruction described above were obtained for

TABLE III. The values of the various efficiency corrections δ_i for the process $e^+e^- \to \Lambda\bar{\Lambda}\gamma$.

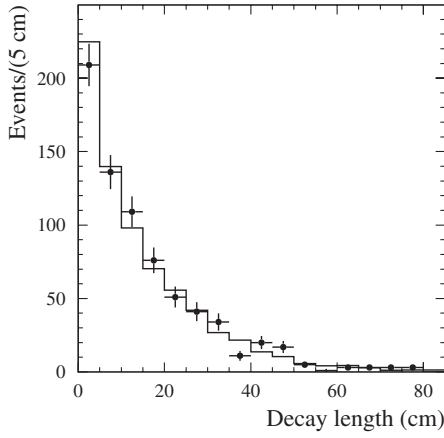| Effect	δ_i, (%)
$\chi^2_{\Lambda\Lambda} < 20$	-2.0 ± 2.0
No identified K	-1.0 ± 1.3
Track reconstruction	-1.0 ± 3.8
$\bar{p}$ nuclear interaction	$+1.0 \pm 0.4$
PID	$+0.6 \pm 0.6$
Photon inefficiency	-1.3 ± 0.3
Photon conversion	$+0.4 \pm 0.2$
Trigger	-0.6 ± 0.5 for $M_{\Lambda\bar{\Lambda}} < 2.4$ GeV/c^2
Total	-3.9 ± 4.6 for $M_{\Lambda\bar{\Lambda}} < 2.4$ GeV/c^2
	-3.3 ± 4.6 for $M_{\Lambda\bar{\Lambda}} > 2.4$ GeV/c^2

FIG. 11. The distribution of Λ flight length for data (points with error bars) and $e^+e^- \to \Lambda\bar{\Lambda}\gamma$ simulation (histogram).

tracks originating from the e^+e^- interaction point. To estimate the possible data-MC simulation difference due to the Λ flight path, we compare the distributions of reconstructed Λ flight length (Fig. 11). The data and simulated distributions are in good agreement, and so there is no need to introduce an extra efficiency correction for this effect.

The data-MC simulation difference for proton identification is calculated using the $p/\bar{p}$ identification probabilities for data and simulation obtained in Ref. [1] for $e^+e^- \to J/\psi\gamma \to p\bar{p}\gamma$.

A correction must be also applied to the photon detection efficiency. There are two main sources for this correction: data-MC simulation difference in the probability of photon conversion in the detector material before the DCH, and the effect of dead calorimeter channels. Both effects

were studied in Ref. [1] using $e^+e^- \to \mu^+\mu^-\gamma$ and $e^+e^- \to \gamma\gamma$ events.

The quality of the simulation of the trigger efficiency was also studied. The overlap of the samples of events passing different trigger criteria and the independence of these triggers were used to measure the trigger efficiency. A small difference [$-(0.6 \pm 0.5)\%$] in trigger efficiency between data and MC simulation was observed for $\Lambda\bar{\Lambda}$ masses below 2.4 GeV/c^2.

The total efficiency correction is $-(3.9 \pm 4.6)\%$ for $M_{\Lambda\bar{\Lambda}} < 2.4$ GeV/c^2 and $-(3.3 \pm 4.6)\%$ for $M_{\Lambda\bar{\Lambda}} > 2.4$ GeV/c^2. The corrected detection efficiencies are listed in Table IV. The uncertainty in detection efficiency includes a simulation statistical error, a model uncertainty, the error on the $\Lambda \to p\pi^-$ branching fraction, and the uncertainty of the efficiency correction.

E. Cross section and form factor

The cross section for $e^+e^- \to \Lambda\bar{\Lambda}$ is calculated from the $\Lambda\bar{\Lambda}$ mass spectrum using the expression

$$\sigma(m) = \frac{(\mathrm{d}N/\mathrm{d}m)_{\mathrm{corr}}}{\varepsilon R \mathrm{d}L/\mathrm{d}m}, \tag{9}$$

where $(\mathrm{d}N/\mathrm{d}m)_{\mathrm{corr}}$ is the mass spectrum corrected for resolution effects, $\mathrm{d}L/\mathrm{d}m$ is the so-called ISR differential luminosity, ε is the detection efficiency as a function of mass, and R is a radiative-correction factor accounting for the Born mass spectrum distortion due to emission of extra photons by the initial electron and positron. The ISR luminosity is calculated using the total integrated luminosity L and the probability density function for ISR photon emission [Eq. (2)]:

TABLE IV. The $\Lambda\bar{\Lambda}$ invariant mass interval ($M_{\Lambda\bar{\Lambda}}$), net number of signal events (N_s), detection efficiency (ε), ISR luminosity (L), measured cross section (σ), and effective form factor (F) for $e^+e^- \to \Lambda\bar{\Lambda}$. The quoted errors on σ are statistical and systematic, respectively. For the form factor, the total error is listed.

$M_{\Lambda\bar{\Lambda}}$ (GeV/c^2)	N_s	ε	L (pb^{-1})	σ (pb)	$|F|$
2.23−2.27	$22.3^{+6.7}_{-6.5}$	0.055 ± 0.006	1.98	$204^{+62}_{-60} \pm 22$	$0.258^{+0.038}_{-0.044}$
2.27−2.30	$24.3^{+6.0}_{-5.8}$	0.057 ± 0.005	2.10	$202^{+50}_{-48} \pm 18$	$0.197^{+0.025}_{-0.027}$
2.30−2.35	$32.6^{+5.8}_{-5.2}$	0.068 ± 0.005	3.06	$155^{+28}_{-25} \pm 12$	$0.154^{+0.014}_{-0.014}$
2.35−2.40	$35.6^{+6.3}_{-6.3}$	0.064 ± 0.005	3.14	$176^{+31}_{-31} \pm 15$	$0.152^{+0.014}_{-0.016}$
2.40−2.45	$19.2^{+6.6}_{-6.4}$	0.066 ± 0.006	3.22	$90^{+31}_{-30} \pm 8$	$0.105^{+0.017}_{-0.020}$
2.45−2.50	$21.4^{+4.8}_{-4.3}$	0.062 ± 0.006	3.30	$104^{+24}_{-21} \pm 10$	$0.110^{+0.013}_{-0.013}$
2.50−2.60	$22.3^{+5.1}_{-4.5}$	0.070 ± 0.005	6.85	$46^{+11}_{-9} \pm 4$	$0.072^{+0.008}_{-0.008}$
2.60−2.70	$11.4^{+5.5}_{-5.9}$	0.064 ± 0.005	7.18	$25^{+12}_{-13} \pm 2$	$0.052^{+0.011}_{-0.016}$
2.70−2.80	$4.7^{+4.0}_{-3.6}$	0.063 ± 0.006	7.52	$10^{+9}_{-8} \pm 1$	$0.033^{+0.012}_{-0.018}$
2.80−3.00	$2.2^{+3.4}_{-3.7}$	0.065 ± 0.006	16.09	$2.1^{+3.2}_{-3.5} \pm 0.2$	$0.016^{+0.009}_{-0.016}$
3.20−3.60	<4.6	0.055 ± 0.005	39.88	<2.1	<0.017
3.80−5.00	<3.9	0.066 ± 0.005	180.38	<0.3	<0.009

$$\frac{dL}{dm} = \frac{\alpha}{\pi x}\left((2 - 2x + x^2)\ln\frac{1 + C}{1 - C} - x^2 C\right)\frac{2m}{s}L. \quad (10)$$

Here $C = \cos\theta_0^*$, and θ_0^* determines the range of polar angles of the ISR photon in the e^+e^- c.m. frame: $\theta_0^* < \theta_\gamma^* < 180° - \theta_0^*$. In our case θ_0^* is equal to $20°$, since we determine efficiency using simulation with $20° < \theta_\gamma^* < 160°$. The values of ISR luminosity integrated over the corresponding mass interval are listed in Table IV.

The radiative-correction factor R is determined using Monte Carlo simulation (at the generator level, with no detector simulation). The $\Lambda\bar{\Lambda}$ mass spectrum is generated using only the pure Born amplitude for the $e^+e^- \to \Lambda\bar{\Lambda}\gamma$ process, and then using a model with next-to-leading-order radiative corrections included. The radiative-correction factor, evaluated as the ratio of the second spectrum to the first, is found to be practically independent of mass, with an average value equal to 1.0035 for masses below 3 GeV/c^2. It should be noted that the value of R depends on the criterion applied to the invariant mass of the $\Lambda\bar{\Lambda}\gamma$ system. The value of R obtained in our case corresponds to the requirement $M_{\Lambda\bar{\Lambda}\gamma} > 8$ GeV/c^2 used in our simulation. The theoretical uncertainty in the radiative-correction calculation is estimated to be less than 1% [8]. The calculated radiative-correction factor does not take into account vacuum polarization, and the contribution of the latter is included in the measured cross section.

The dependence of the mass resolution on the $\Lambda\bar{\Lambda}$ invariant mass is shown in Fig. 12. The mass resolution is calculated in simulation as the rms deviation of the $M_{\Lambda\bar{\Lambda}} - M_{\Lambda\bar{\Lambda}}^{\text{true}}$ distribution. Since the chosen $M_{\Lambda\bar{\Lambda}}$ intervals significantly exceed the mass resolution for all masses, we do not correct the mass spectrum for resolution effects.

The measured cross section for $e^+e^- \to \Lambda\bar{\Lambda}$ is shown in Fig. 13 and listed in Table IV. The quoted errors are

FIG. 13 (color online). The $e^+e^- \to \Lambda\bar{\Lambda}$ cross section measured in the present experiment compared to the DM2 [6] measurement.
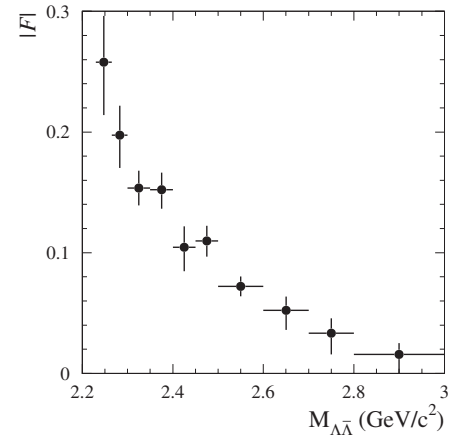
FIG. 14. The measured Λ effective form factor.

statistical and systematic. The latter includes the systematic uncertainty in detection efficiency, the uncertainty in total integrated luminosity (1%), and the uncertainty in the radiative correction (1%). The only previous measurement of the $e^+e^- \to \Lambda\bar{\Lambda}$ cross section, 100^{+65}_{-35} pb at 2.386 GeV [6], is in agreement with our results.

The $e^+e^- \to \Lambda\bar{\Lambda}$ cross section is a function of two form factors. Because of the poorly determined $|G_E/G_M|$ ratio they cannot be extracted from the data simultaneously with reasonable accuracy. We introduce an effective form factor [Eq. (4)] which is a linear combination of $|G_E|^2$ and $|G_M|^2$. The calculated effective form factor is shown in Fig. 14 and listed in Table IV.

F. J/ψ and $\psi(2S)$ decays into $\Lambda\bar{\Lambda}$

The differential cross section for ISR production of a narrow resonance (vector meson V), such as J/ψ, decaying into the final state f can be calculated using [20]
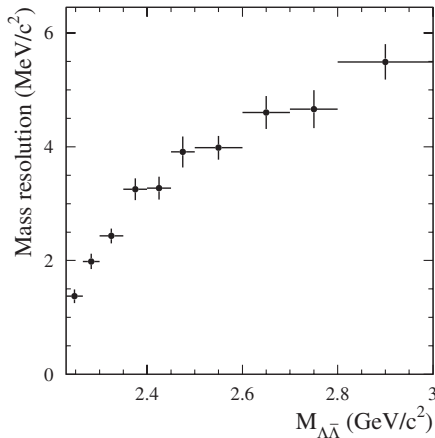

FIG. 12. The mass dependence of the mass resolution calculated as the rms of the $M_{\Lambda\bar{\Lambda}} - M_{\Lambda\bar{\Lambda}}^{\text{true}}$ distribution in MC simulation.
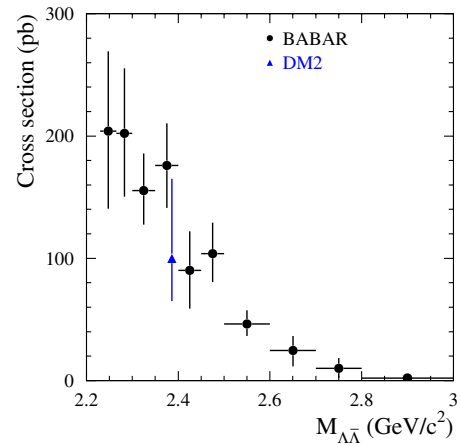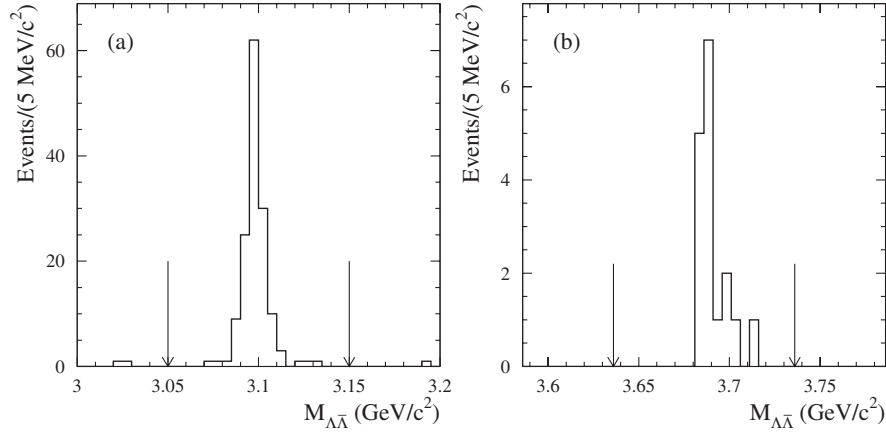
FIG. 15.　The $\Lambda\bar{\Lambda}$ mass spectra in the mass regions near the J/ψ (a) and the $\psi(2S)$ (b). The arrows indicate the boundaries between the signal regions and sidebands.

$$\frac{\mathrm{d}\sigma(s, \theta_\gamma^*)}{\mathrm{d}\cos\theta_\gamma^*} = \frac{12\pi^2\Gamma(V \to e^+e^-)\mathcal{B}(V \to f)}{m_V s} W(s, x_0, \theta_\gamma^*),$$

(11)

where m_V and $\Gamma(V \to e^+e^-)$ are the mass and electronic width of the vector meson V, $x_0 = 1 - m_V^2/s$, and $\mathcal{B}(V \to f)$ is the branching fraction of V into the final state f. Therefore, the measurement of the number of $J/\psi \to \Lambda\bar{\Lambda}$ decays in $e^+e^- \to \Lambda\bar{\Lambda}\gamma$ determines the product of the electronic width and the branching fraction: $\Gamma(J/\psi \to e^+e^-)\mathcal{B}(J/\psi \to \Lambda\bar{\Lambda})$.

The $\Lambda\bar{\Lambda}$ mass spectra for selected events in the J/ψ and $\psi(2S)$ mass regions are shown in Fig. 15. We determine the number of resonance events by counting the events in the signal region indicated in Fig. 15, and subtracting the number in the two sidebands. The following numbers of J/ψ and $\psi(2S)$ events are obtained: $N_{J/\psi} = 142 \pm 12$ and $N_{\psi(2S)} = 17 \pm 4$. A possible background due to $\psi \to p\bar{p}\pi^+\pi^-$ decay is estimated using the two-dimensional distribution of the masses of Λ and $\bar{\Lambda}$ candidates. It is found to be $0.5^{+3.4}_{-0.5}$ events for J/ψ and negligible for $\psi(2S)$.

The detection efficiency is estimated from MC simulation. The event generator uses the experimental data for the angular distribution of the Λ in $J/\psi \to \Lambda\bar{\Lambda}$ decay. This distribution is described by $1 + \alpha\cos^2\theta$ with $\alpha = 0.65 \pm 0.010$ [14–16]. For the $\psi(2S)$ the value $\alpha = 0.69$ predicted in [21] is used. The error in the detection efficiency due to the uncertainty of α is negligible for the J/ψ and is taken to be 5% for the $\psi(2S)$. The efficiencies corrected for data-MC simulation differences are 0.062 ± 0.004 for the J/ψ and 0.059 ± 0.005 for the $\psi(2S)$.

The cross section for $e^+e^- \to \psi\gamma \to \Lambda\bar{\Lambda}\gamma$ for $20° < \theta_\gamma^* < 160°$ is calculated as

$$\sigma(20° < \theta_\gamma^* < 160°) = \frac{N_\psi}{\varepsilon R L},$$

(12)

yielding $(9.8 \pm 0.9 \pm 0.6)$ fb and $(1.2 \pm 0.3 \pm 0.1)$ fb for the J/ψ and $\psi(2S)$, respectively. The radiative-correction factor $R = \sigma/\sigma_{\text{Born}}$ is 1.007 ± 0.010 for the J/ψ and 1.011 ± 0.010 for the $\psi(2S)$, obtained from MC simulation at the generator level.

The total integrated luminosity for the data sample is (230 ± 2) fb^{-1}. From the measured cross sections and Eq. (11), the following products are determined:

$$\Gamma(J/\psi \to e^+e^-)\mathcal{B}(J/\psi \to \Lambda\bar{\Lambda}) = (10.7 \pm 0.9 \pm 0.7)\,\text{eV},$$

$$\Gamma(\psi(2S) \to e^+e^-)\mathcal{B}(\psi(2S) \to \Lambda\bar{\Lambda}) = (1.5 \pm 0.4 \pm 0.1)\,\text{eV}.$$

The systematic errors include the uncertainties in detection efficiency, integrated luminosity, and the radiative correction.

Using the world-average values of the electronic widths [13], the $\psi \to \Lambda\bar{\Lambda}$ branching fractions are calculated to be

$$\mathcal{B}(J/\psi \to \Lambda\bar{\Lambda}) = (1.92 \pm 0.21) \times 10^{-3},$$

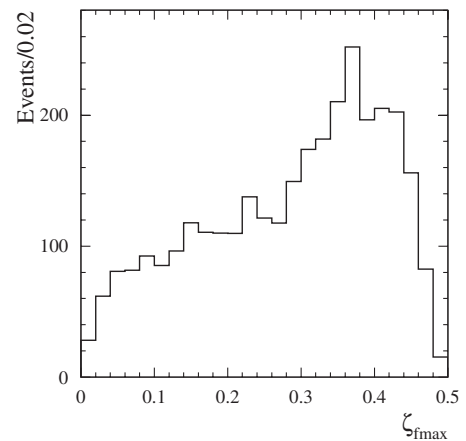$$\mathcal{B}(\psi(2S) \to \Lambda\bar{\Lambda}) = (6.0 \pm 1.5) \times 10^{-4}.$$

FIG. 16.　The distribution of $\zeta_{f\,\text{max}}$ for selected simulated events for $e^+e^- \to \Lambda\bar{\Lambda}\gamma$ with $M_{\Lambda\bar{\Lambda}} < 2.8$ GeV/c^2.

Both results are higher than the current world-average values [13], $(1.54 \pm 0.19) \times 10^{-3}$ and $(2.5 \pm 0.7) \times 10^{-4}$, but in reasonable agreement with the more precise recent measurements, $(2.03 \pm 0.15) \times 10^{-3}$ by BES [16] and $(3.33 \pm 0.25) \times 10^{-4}$ by CLEO [22] and BES [23].

G. Measurement of the Λ polarization

A nonzero relative phase ϕ between the electric and magnetic form factors leads to polarization of the outgoing baryons. The exact formula for the Λ ($\bar{\Lambda}$) polarization vector ζ_f is given in the Appendix. The polarization is proportional to $\sin\phi$. The magnitude of the polarization $\zeta_{f\,\text{max}} = \zeta_f(\phi = \pi/2)$ calculated under the assumption that $|G_E| = |G_M|$ for simulated $e^+e^- \to \Lambda\bar{\Lambda}\gamma$ events with $M_{\Lambda\bar{\Lambda}} < 2.8$ GeV/c^2 is shown in Fig. 16. The simulated events were reweighted according to the $\Lambda\bar{\Lambda}$ mass spectrum observed in data. The average value of $\zeta_{f\,\text{max}}$ is equal to 0.285. The Λ polarization can be measured using the correlation between the direction of the Λ polarization vector and the direction of the proton from Λ decay:

$$\frac{dN}{d\cos\theta_{p\zeta}} = A(1 + \alpha_\Lambda \zeta_f \cos\theta_{p\zeta}), \qquad (13)$$

where $\theta_{p\zeta}$ is the angle between the polarization axis and the proton momentum in the Λ rest frame, and $\alpha_\Lambda = 0.642 \pm 0.013$ [13]. For $\bar{\Lambda}$, $\alpha_{\bar{\Lambda}} = -\alpha_\Lambda$. The distribution of $\cos\theta_{p\zeta}$ for simulated $e^+e^- \to \Lambda\bar{\Lambda}\gamma$ events with $M_{\Lambda\bar{\Lambda}} < 2.8$ GeV/c^2 (there is no Λ polarization in the simulation) is shown in Fig. 17(a). We combine the Λ and $\bar{\Lambda}$ distributions taking into account the different signs of α_Λ and $\alpha_{\bar{\Lambda}}$. Since the distribution is flat, we conclude that there is no dependence of the detection efficiency on $\cos\theta_{p\zeta}$. A fit to the distribution using a linear function gives slope consistent with zero.

The same distribution for data is shown in Fig. 17(b). In each angular interval the background is subtracted using the procedure described in Sec. III B. The distribution is fitted using a linear function. The slope is found to be 0.020 ± 0.097. The corresponding symmetric 90% CL interval for Λ polarization averaged over the $\Lambda\bar{\Lambda}$ mass range from threshold to 2.8 GeV/c^2 is

$$-0.22 < \zeta_f < 0.28.$$

Under the assumption $|G_E| = |G_M|$ ($\bar{\zeta}_{f\,\text{max}} = 0.285$), which does not contradict the data, this interval can be converted to an interval for $\sin\phi$ as follows:

$$-0.76 < \sin\phi < 0.98.$$

Our statistics allow only very weak limits to be set on $\sin\phi$.

IV. THE REACTION $e^+e^- \to \Sigma^0\bar{\Sigma}^0\gamma$

A. Event selection

The Σ^0 hyperons are detected via the decay $\Sigma^0 \to \Lambda\gamma$ (the branching fraction is 100% [13]). Therefore, the preliminary selection of $e^+e^- \to \Sigma^0\bar{\Sigma}^0\gamma$ candidate events is similar to that for $e^+e^- \to \Lambda\bar{\Lambda}\gamma$. In addition, we require that an event contain at least two extra photons with energy greater than 30 MeV. To suppress combinatorial background from events not containing two Λ's in the final state, we apply a tighter selection criterion on the mass of a Λ ($\bar{\Lambda}$) candidate: $1.110 < M_{p\pi^-} < 1.122$ GeV/c^2.

For events passing the preliminary selection, we perform a kinematic fit to the $e^+e^- \to \Lambda\bar{\Lambda}\gamma\gamma\gamma$ hypothesis. The photon with highest E_γ^* is assumed to be the ISR photon. The fitted momenta of two other photons and Λ baryons are used to calculate $\Lambda\gamma$ and $\bar{\Lambda}\gamma$ invariant masses. For Σ^0 and $\bar{\Sigma}^0$ candidates these masses must be in the range 1.155–1.23 GeV/c^2 [the nominal $\bar{\Sigma}^0$ mass is $1.192642(24)$ GeV/c^2 [13]]. We require that an event contain at least one Σ^0 and one $\bar{\Sigma}^0$ candidate. For events with
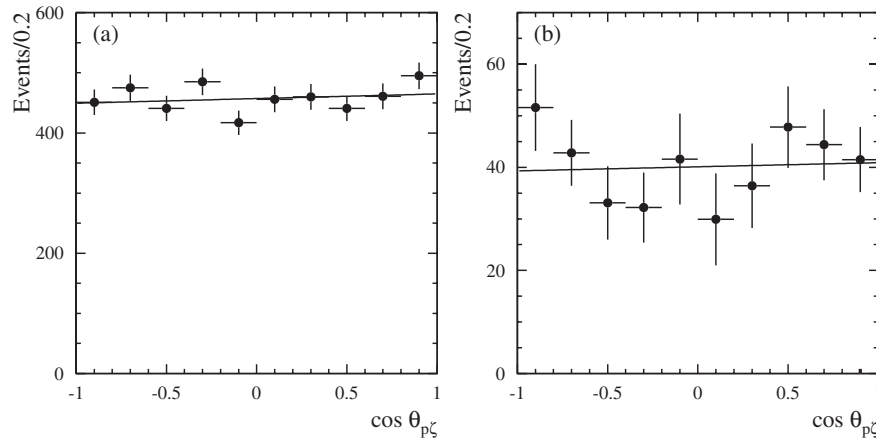

FIG. 17.   The distribution of $\cos\theta_{p\zeta}$ for selected $e^+e^- \to \Lambda\bar{\Lambda}\gamma$ events with $M_{\Lambda\bar{\Lambda}} < 2.8$ GeV/c^2 in simulation (a) and in data (b).
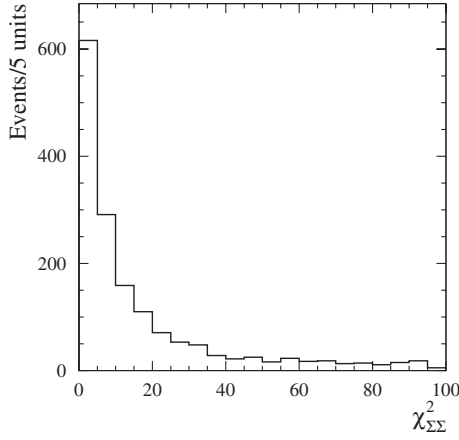
FIG. 18. The $\chi^2_{\bar{\Sigma}\Sigma}$ distributions for simulated events for $e^+e^- \to \Sigma^0\bar{\Sigma}^0\gamma$.

FIG. 19. The $\chi^2_{\Lambda\Lambda}$ distributions for simulated events for $e^+e^- \to \Lambda\bar{\Lambda}\gamma$ (solid histogram) and $e^+e^- \to \Sigma^0\bar{\Sigma}\gamma$ (dashed histogram).

FIG. 20. The $\chi^2_{\Lambda\Sigma}$ distributions for simulated events for $e^+e^- \to \Lambda\bar{\Sigma}^0\gamma$ (solid histogram) and $e^+e^- \to \Sigma^0\bar{\Sigma}^0\gamma$ (dashed histogram).

more than three photons we iterate over all possible photon combinations and find the one containing Σ^0 and $\bar{\Sigma}^0$ candidates and giving the lowest χ^2 for the kinematic fit.

The distribution of the χ^2 of the kinematic fit ($\chi^2_{\bar{\Sigma}\Sigma}$) for simulated $e^+e^- \to \Sigma^0\bar{\Sigma}^0\gamma$ events is shown in Fig. 18. We select data events with $\chi^2_{\bar{\Sigma}\Sigma} < 20$ for further analysis; as before, a χ^2 control region ($20 < \chi^2_{\bar{\Sigma}\Sigma} < 40$) is used for background estimation and subtraction.

To suppress background from $e^+e^- \to \Lambda\bar{\Lambda}\gamma$ and $e^+e^- \to \Lambda\bar{\Sigma}^0\gamma$ events with extra photons, we also perform kinematic fits to the $\Lambda\bar{\Lambda}\gamma$ and $\Lambda\bar{\Sigma}^0\gamma$ hypotheses. The $\Lambda\bar{\Sigma}^0\gamma$ fit is a fit to the $e^+e^- \to \Lambda\bar{\Lambda}\gamma\gamma$ hypothesis. The photon with highest E^*_γ is assumed to be the ISR photon. The other photon taken in combination with the Λ or $\bar{\Lambda}$ must give an invariant mass value in the range 1.155–1.23 GeV/c^2, where the mass is calculated using fitted momenta. The $\chi^2_{\Lambda\Lambda}$ distributions for simulated events corresponding to $e^+e^- \to \Lambda\bar{\Lambda}\gamma$ and $e^+e^- \to \Sigma^0\bar{\Sigma}^0\gamma$ are shown in Fig. 19. The requirement $\chi^2_{\Lambda\Lambda} > 20$ rejects 93% of $\Lambda\bar{\Lambda}\gamma$ events and only 3% of signal events. Similarly, the $\chi^2_{\Lambda\Sigma}$ distributions for simulated events for $e^+e^- \to \Lambda\bar{\Sigma}^0\gamma$ and $e^+e^- \to \Sigma^0\bar{\Sigma}^0\gamma$ are shown in Fig. 20. The requirement $\chi^2_{\Lambda\Sigma} > 20$ again rejects 93% of $\Lambda\bar{\Sigma}^0\gamma$ events, but in this case removes 30% of the signal events. Data events with $\chi^2_{\Lambda\Sigma} < 20$ are used to estimate the level of $\Lambda\bar{\Sigma}^0\gamma$ background.

The scatter plots of the invariant mass of the Σ^0 candidate versus the invariant mass of the $\bar{\Sigma}^0$ candidate for the selected data events and simulated $e^+e^- \to \Sigma^0\bar{\Sigma}^0\gamma$ events are shown in Figs. 21(a) and 21(b), respectively. Of the two possible $\Lambda\gamma$ and $\bar{\Lambda}\gamma$ combinations, we plot only the combination with the smaller value of $(M_{\Lambda\gamma} - m_\Sigma)^2 + (M_{\bar{\Lambda}\gamma} - m_{\bar{\Sigma}})^2$, where m_Σ is the nominal Σ^0 mass.

The $\Sigma^0\bar{\Sigma}^0$ mass spectrum for the data events, with the additional requirement that the Σ^0 and $\bar{\Sigma}^0$ candidate mass
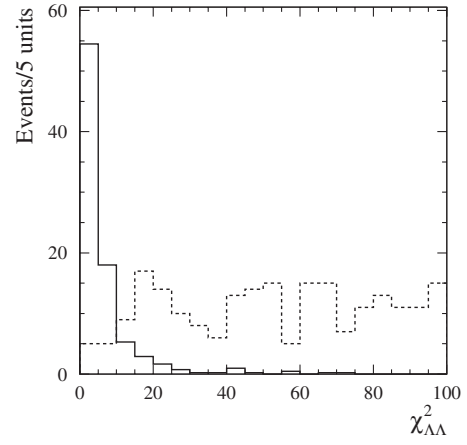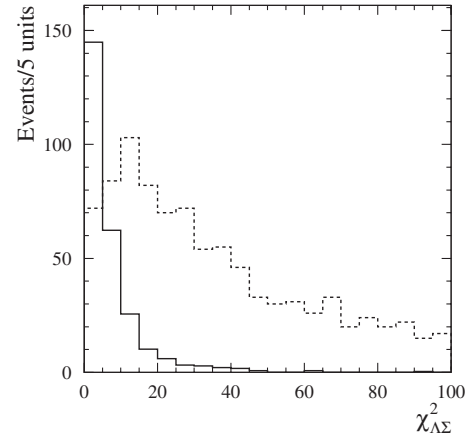
values satisfy $1.180 < M_{\Lambda\gamma} < 1.205$ GeV/c^2 [central box in Fig. 21(a)], is shown in Fig. 22.

An excess of signal events is seen at masses below 3.0 GeV/c^2. There are also about 20 events near the J/ψ mass, corresponding to $J/\psi \to \Sigma^0\bar{\Sigma}^0$ decay. The two events near 3.7 GeV/c^2 may be due to $\psi(2S) \to \Sigma^0\bar{\Sigma}^0$ decay. The mass distribution for Σ^0 and $\bar{\Sigma}^0$ candidates from the J/ψ region is shown in Fig. 23. The spectrum is obtained as the difference of the spectrum from the region $3.05 < M_\Sigma < 3.15$ GeV/c^2 and that from the sideband region (3.00–3.05 and 3.15–3.20 GeV/c^2). We see that simulation reproduces the Σ^0 line shape quite well.

B. Background subtraction

Background processes can be divided into three classes, namely, those with zero ($e^+e^- \to \Lambda\bar{\Lambda}\gamma$, $\Lambda\bar{\Lambda}\pi^0$, $\Lambda\bar{\Lambda}\pi^0\gamma$, ...), one ($e^+e^- \to \Lambda\bar{\Sigma}^0\gamma$, $\Lambda\bar{\Sigma}^0\pi^0$, $\Lambda\bar{\Sigma}^0\pi^0\gamma$, ...), and two
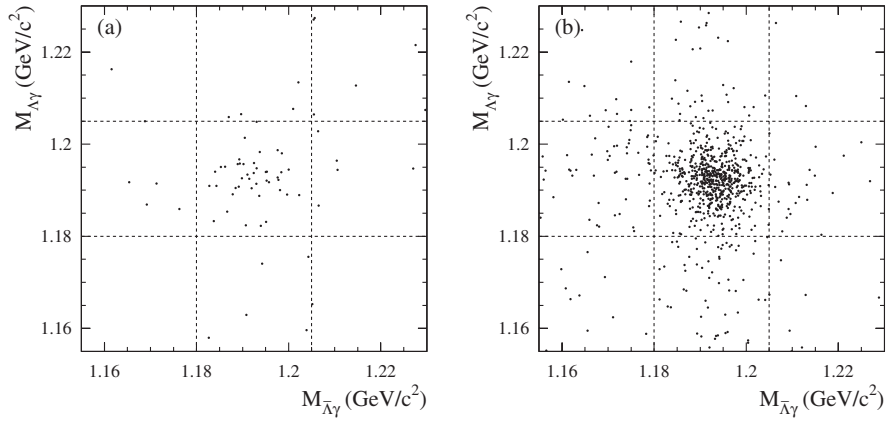
FIG. 21. Scatter plots of the invariant mass of the Σ^0 candidate versus the invariant mass of the $\bar{\Sigma}^0$ candidate for selected data events (a) and simulated $e^+e^- \rightarrow \Sigma^0\bar{\Sigma}^0\gamma$ events (b).

Σ^0's ($e^+e^- \rightarrow \Sigma^0\bar{\Sigma}^0\pi^0, \Sigma^0\bar{\Sigma}^0\pi^0\gamma, \ldots$) in the final state. To separate events with two Σ^0's from events with no Σ^0's and one Σ^0, we use the differences in their two-dimensional distributions of invariant mass values of the Σ^0 and $\bar{\Sigma}^0$ candidates.

Background events from $e^+e^- \rightarrow \Sigma^0\bar{\Sigma}^0\pi^0$ with an undetected low-energy photon or with merged photons from π^0 decay yield a low value of χ^2 when reconstructed under the $\Sigma^0\bar{\Sigma}^0\gamma$ hypothesis, and cannot be separated from the process under study. Special selection procedures are applied in order to estimate this background. The procedures are similar to those used to study background from $e^+e^- \rightarrow \Lambda\bar{\Lambda}\pi^0$ in Sec. III B. No $\Sigma^0\bar{\Sigma}^0\pi^0$ candidates are found in data, and we estimate that the background from this process does not exceed five events. Assuming that the dibaryon mass spectrum in $e^+e^- \rightarrow \Sigma^0\bar{\Sigma}^0\pi^0$ is similar to that for $e^+e^- \rightarrow p\bar{p}\pi^0$ [1], we find that about 70% of the $e^+e^- \rightarrow \Sigma^0\bar{\Sigma}^0\pi^0$ events are expected to have $\Sigma^0\bar{\Sigma}^0$ mass less than 3 GeV/c^2. Two-Σ^0 background other than that from $\Sigma^0\bar{\Sigma}^0\pi^0$ can be estimated using the difference in the χ^2 distributions for signal and background events.
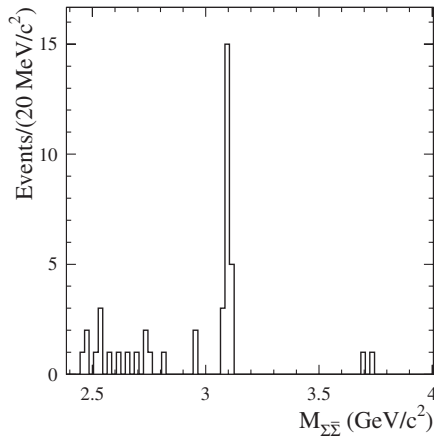
The 3×3 two-dimensional histograms of $M_{\Lambda\gamma}$ vs $M_{\bar{\Lambda}\gamma}$ (dashed lines in Fig. 21) for events from three classes,

$$\chi^2_{\Sigma\Sigma} < 20, \quad \chi^2_{\Lambda\Sigma} > 20,$$
$$20 < \chi^2_{\Sigma\Sigma} < 40, \quad \chi^2_{\Lambda\Sigma} > 20,$$
$$\chi^2_{\Sigma\Sigma} < 20, \quad \chi^2_{\Lambda\Sigma} < 20,$$

are fitted simultaneously. The second histogram is used to determine two-Σ^0 background. From the third histogram we estimate the $e^+e^- \rightarrow \Lambda\bar{\Sigma}^0\gamma$ background. Each histogram is fitted using the following function:

$$N_{ij} = N_2 f^{2\Sigma}_{i,j} + N_1 f^{1\Sigma}_{i,j} + N_0 f^{0\Sigma}_{i,j},$$

where N_0, N_1, and N_2 are the numbers of events with zero, one, and two Σ^0's in the final state. The functions $f^{1\Sigma}$ and $f^{2\Sigma}$ are taken from $e^+e^- \rightarrow \Lambda\bar{\Sigma}^0\gamma$ and $e^+e^- \rightarrow \Sigma^0\bar{\Sigma}^0\gamma$ simulations. The probability density function for zero-Σ^0 events is the product of two identical linear functions of

FIG. 22. The $\Sigma^0\bar{\Sigma}^0$ mass spectrum for the selected data events.
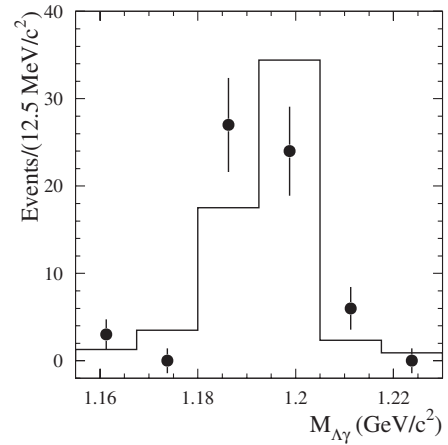

FIG. 23. The $\Lambda\gamma$ and $\bar{\Lambda}\gamma$ invariant mass distribution for data (points with error bars) and simulated (histogram) events from the J/ψ region.

TABLE V. Comparison of the fit results for $\Sigma^0\bar{\Sigma}^0$ masses below 3 GeV/c^2 and the predictions from JETSET simulation; N_{2s}, N_0, N_1, N_{2b} are the fitted numbers of signal, zero-, one-, and two-Σ^0 background events in the signal region ($\chi^2_{\Sigma\Sigma} < 20$, $\chi^2_{\Lambda\Sigma} > 20$), respectively, and $N_{\Sigma^0\bar{\Sigma}^0\pi^0}$ is the expected number of background events from the $e^+e^- \to \Sigma^0\bar{\Sigma}^0\pi^0$ process.

	N_{2s}	N_0	N_1	N_{2b}	$N_{\Sigma^0\bar{\Sigma}^0\pi^0}$
Data	$18.1^{+7.8}_{-7.5}$	11.3 ± 4.8	1.2 ± 0.6	2.8 ± 4.8	<4
JETSET	33 ± 5	3.1 ± 1.4	1.2 ± 0.8	<1.4	0.6 ± 0.6

TABLE VI. The values of the various efficiency corrections for the process $e^+e^- \to \Sigma^0\bar{\Sigma}^0\gamma$.

Effect	δ_i, (%)
$\chi^2_{\Sigma\Sigma} < 20$	-2.0 ± 6.0
Track reconstruction	-1.0 ± 3.8
$\bar{p}$ nuclear interaction	$+1.0 \pm 0.4$
PID	$+0.6 \pm 0.6$
Photon inefficiency	-3.9 ± 0.9
Photon conversion	$+1.2 \pm 0.6$
Total	-4.1 ± 7.2

$M_{\Lambda\gamma}$ and $M_{\bar{\Lambda}\gamma}$ and a function taking into account the correlation between masses of the Σ^0 and $\bar{\Sigma}^0$ candidates. This last function is extracted from $e^+e^- \to \Lambda\bar{\Lambda}\gamma$ simulation. The correlation arises from our choice of one of the two possible combinations of Λ and $\bar{\Lambda}$ candidates with photons, and is about 15% for the central mass bin.

In order to find the number of signal events and estimate the background, we use the following relations:

$$N_2(\chi^2_{\Sigma\Sigma} < 20, \chi^2_{\Lambda\Sigma} > 20) = N_{2s} + N_{2b},$$
$$N_2(20 < \chi^2_{\Sigma\Sigma} < 40, \chi^2_{\Lambda\Sigma} > 20) = \alpha_1 N_{2s} + \beta_1 N_{2b},$$
$$N_2(\chi^2_{\Sigma\Sigma} < 20, \chi^2_{\Lambda\Sigma} < 20) = \alpha_2 N_{2s} + \beta_2 N_{2b},$$
$$N_1(\chi^2_{\Sigma\Sigma} < 20, \chi^2_{\Lambda\Sigma} > 20) = N_{1s} + N_{1b},$$
$$N_1(20 < \chi^2_{\Sigma\Sigma} < 40, \chi^2_{\Lambda\Sigma} > 20) = \gamma_1 N_{1s} + \delta_1 N_{1b},$$
$$N_1(\chi^2_{\Sigma\Sigma} < 20, \chi^2_{\Lambda\Sigma} < 20) = \gamma_2 N_{1s} + \delta_2 N_{1b},$$

where N_{2s} is the number of signal $\Sigma^0\bar{\Sigma}^0\gamma$ events and N_{2b} is the number of two-Σ^0 background events in the signal region ($\chi^2_{\Sigma\Sigma} < 20$, $\chi^2_{\Lambda\Sigma} > 20$); N_{1s} is the number of $\Lambda\bar{\Sigma}^0\gamma$ events and N_{1b} is the number of one-Σ^0 events from all other processes in the signal region; N_{2s}, N_{2b}, N_{1s}, and N_{1b} are then free fit parameters. The coefficients $\alpha_i, \beta_i, \gamma_i$, and δ_i are obtained from simulation of $e^+e^- \to \Sigma^0\bar{\Sigma}^0\gamma$, $e^+e^- \to \Sigma^0\bar{\Sigma}^0\pi^0\gamma$, $e^+e^- \to \Lambda\bar{\Sigma}^0\gamma$, $e^+e^- \to \Lambda\bar{\Sigma}^0\pi^0\gamma$, respectively. For the coefficients most critical to the analysis, $\alpha_1 = 0.22 \pm 0.03$ and $\beta_1 = 1.5 \pm 0.3$, the errors include uncertainties due to the data-MC difference in the χ^2 distributions for the kinematic fits. The other six free parameters are the numbers of zero-Σ^0 events in the three histograms, and the slopes of the linear functions describing the mass distributions for these events.

The fit results for $\Sigma^0\bar{\Sigma}^0$ masses below 3 GeV/c^2 are shown in Table V, together with the predictions from JETSET simulation. The one-Σ^0 background is dominated by the $e^+e^- \to \Lambda\bar{\Sigma}^0\gamma$ process. The number of one-Σ^0 events from other processes is found to be consistent with zero. The numbers of $e^+e^- \to \Sigma^0\bar{\Sigma}^0\gamma$ and $e^+e^- \to \Lambda\bar{\Sigma}^0\gamma$ events with $\chi^2_{\Lambda\Sigma} < 20$ are $7.7^{+3.4}_{-3.2}$ and $15.3^{+5.4}_{-7.7}$, respectively.

The fitting procedure was performed in five $\Sigma^0\bar{\Sigma}^0$ mass ranges, and the number of signal events found in each is listed in Table VII. For $\Sigma^0\bar{\Sigma}^0$ masses below 3 GeV/c^2 we observe an excess of signal events over background. The significance of the observation of $\Sigma^0\bar{\Sigma}^0$ production in the mass region below 3.0 GeV/c^2 is 2.9σ. For other mass bins we list upper limits at the 90% CL.

C. Cross section and form factor

The cross section for $e^+e^- \to \Sigma^0\bar{\Sigma}^0$ is calculated from the $\Sigma^0\bar{\Sigma}^0$ mass spectrum according to Eqs. (9) and (10).

The detection efficiency is determined from MC simulation and then corrected for data-MC simulation differences in detector response. The model dependence of the detection efficiency due to the unknown $|G_E/G_M|$ ratio is estimated to be 5% (see Sec. III D). The efficiency corrections summarized in Table VI were discussed in Sec. III D.

TABLE VII. The $\Sigma^0\bar{\Sigma}^0$ invariant mass interval ($M_{\Sigma\bar{\Sigma}}$), net number of signal events (N_s), detection efficiency (ε), ISR luminosity (L), measured cross section (σ), and effective form factor (F) for $e^+e^- \to \Sigma^0\bar{\Sigma}^0$. The quoted errors on σ are statistical and systematic. For the form factor, the total error is listed.

$M_{\Sigma\bar{\Sigma}}$ (GeV/c^2)	N_s	ε	L (pb^{-1})	σ (pb)	$|F|$
2.385–2.600	$10.3^{+4.4}_{-4.5}$	0.024 ± 0.002	14.3	$30 \pm 13 \pm 3$	$0.090^{+0.018}_{-0.023}$
2.600–2.800	$6.5^{+3.1}_{-3.8}$	0.025 ± 0.003	14.7	$17^{+8}_{-10} \pm 2$	$0.047^{+0.010}_{-0.017}$
2.800–3.000	$1.4^{+3.5}_{-3.2}$	0.026 ± 0.003	16.1	$3.4^{+8.5}_{-7.8} \pm 0.4$	$0.021^{+0.018}_{-0.021}$
3.200–3.600	<2.3	0.023 ± 0.003	39.9	<2.5	<0.019
3.800–5.000	<2.3	0.023 ± 0.002	180.4	<0.5	<0.011

On the basis of our analysis of ISR processes with photons in the final state [24], we enlarge the systematic error in the correction for the χ^2 selection interval. The correction for trigger inefficiency is removed, since for $e^+e^- \to \Sigma^0\bar{\Sigma}^0\gamma$, trigger inefficiency is less than 0.001 both in data and in MC simulation. The corrected detection efficiencies are listed in Table VII. The overall uncertainty in efficiency takes into account simulation statistical error, model uncertainty, the error in the $\Lambda \to p\pi^-$ branching fraction, and the uncertainty of the efficiency correction.

The measured values of the $e^+e^- \to \Sigma^0\bar{\Sigma}^0$ cross section are listed in Table VII, together with the effective form factor values calculated according to Eq. (4). The quoted errors on the cross section are statistical and systematic. The latter includes systematic uncertainty in detection efficiency, the uncertainty in total integrated luminosity (1%), and radiative-correction uncertainty (1%). This is the first measurement of the $e^+e^- \to \Sigma^0\bar{\Sigma}^0$ cross section. The upper limit set by DM2 [6] at 2.386 GeV (< 120 pb) is consistent with our measurements.

D. J/ψ decay into $\Sigma^0\bar{\Sigma}^0$

The $\Sigma^0\bar{\Sigma}^0$ mass spectrum for selected events in the J/ψ mass region is shown in Fig. 24. We determine the number of resonance events by counting the events in the signal region indicated in Fig. 24 and subtracting the number in the two sidebands. The net number of J/ψ decay events is then 30 ± 6.

The detection efficiency is estimated from MC simulation. The event generator uses the experimental data on the Σ^0 angular distribution in $J/\psi \to \Sigma^0\bar{\Sigma}^0$ decay, which is $1 + \alpha\cos^2\theta$ with $\alpha = -0.1 \pm 0.2$ [14–16]. The error in the detection efficiency due to the uncertainty in α is negligible. The efficiency corrected for data-MC simulation differences is $\varepsilon = 0.022 \pm 0.002$.

Using Eqs. (11) and (12), the following product is determined:

$$\Gamma(J/\psi \to e + e-)\mathcal{B}(J/\psi \to \Sigma^0\bar{\Sigma}^0)$$
$$= (6.4 \pm 1.2 \pm 0.6) \text{ eV}.$$

The systematic error includes the uncertainties in detection efficiency, integrated luminosity, and in the radiative correction. Using the PDG value of the electronic width [13], the $J/\psi \to \Sigma^0\bar{\Sigma}^0$ branching fraction is calculated to be

$$\mathcal{B}(J/\psi \to \Sigma^0\bar{\Sigma}^0) = (1.16 \pm 0.26) \times 10^{-3}.$$

Our result is in agreement with the world-average value $(1.31 \pm 0.10) \times 10^{-3}$ [13].

We also observe two events in the $\psi(2S)$ region with zero background, estimated from the sidebands. This number agrees with the 2.5 ± 0.4 events expected from the measured branching fraction $\mathcal{B}(\psi(2S) \to \Sigma^0\bar{\Sigma}^0) = (2.51 \pm 0.31) \times 10^{-4}$ [22,23].

V. THE REACTION $e^+e^- \to \Lambda\bar{\Sigma}^0\gamma$

A. Event selection

The preliminary selection of $e^+e^- \to \Lambda\bar{\Sigma}^0\gamma$ events is similar to that for $e^+e^- \to \Lambda\bar{\Lambda}\gamma$. Additionally we require that an event candidate contain at least one extra photon with energy greater than 30 MeV. To suppress combinatorial background from events not containing two Λ's in the final state, we require that the mass of the Λ ($\bar{\Lambda}$) satisfy $1.110 < M_{p\pi^-} < 1.122$ GeV/c^2.

For events passing the preliminary selection, we perform a kinematic fit to the $e^+e^- \to \Lambda\bar{\Sigma}^0\gamma$ hypothesis as described in Sec. IVA. The $\chi^2_{\Lambda\Sigma}$ distribution for simulated $\Lambda\bar{\Sigma}^0\gamma$ events is shown in Fig. 25. We select the events with $\chi^2_{\Lambda\Sigma} < 20$ for further analysis. The control region ($20 < \chi^2_{\Lambda\Sigma} < 40$) is used for background estimation and subtraction.

To suppress background resulting from $e^+e^- \to \Lambda\bar{\Lambda}\gamma$ events with an additional photon, we perform a kinematic
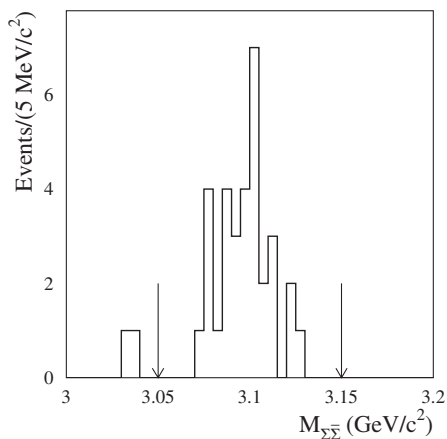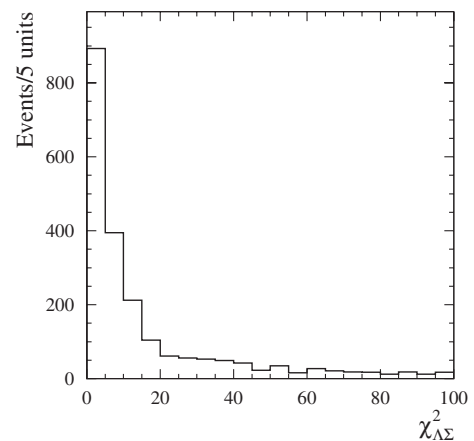

FIG. 24. The $\Sigma^0\bar{\Sigma}^0$ mass spectrum for the mass region near the J/ψ. The arrows indicate the boundaries between the signal region and sideband regions.

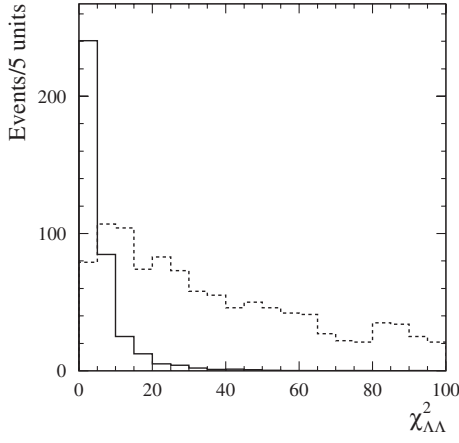FIG. 25. The $\chi^2_{\Lambda\Sigma}$ distributions for simulated $e^+e^- \to \Lambda\bar{\Sigma}^0\gamma$ events.

FIG. 26. The $\chi^2_{\Lambda\Lambda}$ distributions for simulated $e^+e^- \to \Lambda\bar{\Lambda}\gamma$ events (solid histogram) and $e^+e^- \to \Lambda\bar{\Sigma}^0\gamma$ events (dashed histogram).

fit to the $\Lambda\bar{\Lambda}\gamma$ hypothesis and require that $\chi^2_{\Lambda\Lambda} > 20$. The $\chi^2_{\Lambda\Lambda}$ distributions for simulated $e^+e^- \to \Lambda\bar{\Lambda}\gamma$ and $e^+e^- \to \Lambda\bar{\Sigma}^0\gamma$ events are shown in Fig. 26. The $\chi^2_{\Lambda\Lambda} > 20$ cut rejects 95% of the $\Lambda\bar{\Lambda}\gamma$ events at the cost of 20% of the signal events.

The distribution of Σ^0 candidate invariant mass for data events passing the $\Lambda\bar{\Sigma}^0\gamma$ selection process is shown in Fig. 27. For each event we plot only the $\Lambda(\bar{\Lambda})\gamma$ combination closer to the nominal Σ^0 mass. The $\Lambda\bar{\Sigma}^0$ mass distribution for selected data events with invariant mass of the $\bar{\Sigma}^0$ candidate in the $1.185 - 1.205$ GeV/c^2 range is shown in Fig. 28. We expect that the $e^+e^- \to \Sigma^0\bar{\Sigma}^0\gamma$ process results in a significant contribution to the selected event sample.

In particular, the peak in the $\Lambda\bar{\Sigma}^0$ mass spectrum near 3 GeV/c^2 is from $J/\psi \to \Sigma^0\bar{\Sigma}^0$ events with a missing or excluded photon.
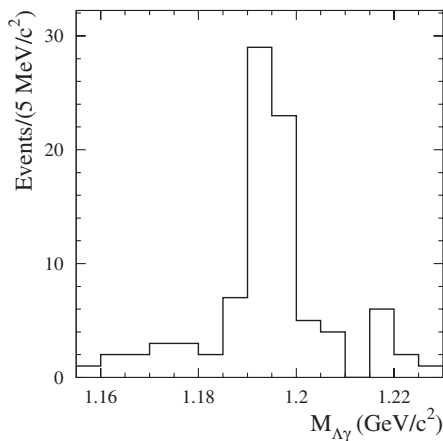

FIG. 27. The distribution of the invariant mass of the Σ^0 and $\bar{\Sigma}^0$ candidates for the selected $\Lambda\bar{\Sigma}^0\gamma$ candidate.
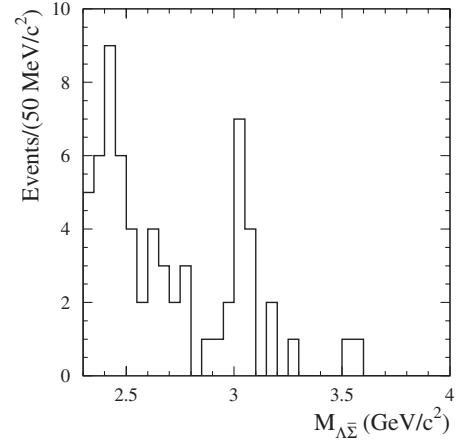

FIG. 28. The $\Lambda\bar{\Sigma}^0$ invariant mass spectrum for data events with the invariant mass of the Σ^0 candidate in the 1.185–1.205 GeV/c^2 range.

B. Background subtraction

The background processes can be divided into three classes, namely, those with zero ($e^+e^- \to \Lambda\bar{\Lambda}\gamma$, $\Lambda\bar{\Lambda}\pi^0$, $\Lambda\bar{\Lambda}\pi^0\gamma$, ...), one ($e^+e^- \to \Lambda\bar{\Sigma}^0\pi^0$, $\Lambda\bar{\Sigma}^0\pi^0\gamma$, ...), and two Σ^0's ($e^+e^- \to \Sigma^0\bar{\Sigma}^0\gamma$, $\Sigma^0\bar{\Sigma}^0\pi^0$, $\Sigma^0\bar{\Sigma}^0\pi^0\gamma$, ...) in the final state. To separate one-Σ^0 events from events with no Σ^0 we use the difference in mass distribution for the respective Σ^0 ($\bar{\Sigma}^0$) candidates.

To determine two-Σ^0 background we select a clean sample of two-Σ^0 events. To do this the $\Sigma^0\bar{\Sigma}^0\gamma$ criteria (Sec. IVA) are used with the additional requirements that $1.180 < M_{\Lambda\gamma} < 1.205$ GeV/c^2 for the Σ^0 and $\bar{\Sigma}^0$ candidates, and that $\chi^2_{\Lambda\Sigma} < 100$. The latter requirement is

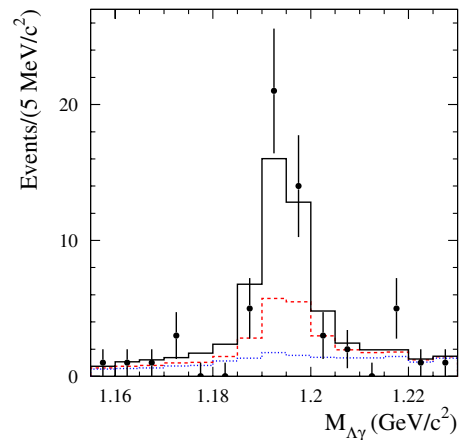FIG. 29 (color online). The distribution of the invariant mass of the Σ^0 ($\bar{\Sigma}^0$) candidate for data events with $M_{\Lambda\bar{\Sigma}} < 2.9$ GeV/c^2 (points with error bars). The solid histogram shows the result of the fit described in the text. The dotted histogram shows the contribution of zero-Σ^0 background. The difference between dashed and dotted histograms is the contribution of two-Σ^0 background.

needed to obtain a useful $M_{\Lambda\bar{\Sigma}}$ distribution. Using the ratio of detection efficiencies for two-Σ^0 and $\Lambda\bar{\Sigma}^0\gamma$ selections ($\kappa = 0.80 \pm 0.05$), we can convert the number of events in the two-Σ^0 sample to an estimate of the number of background events in the $\Lambda\bar{\Sigma}^0\gamma$ sample.

The background from $e^+e^- \to \Lambda\bar{\Sigma}^0\pi^0$ events with an undetected low-energy photon or with merged photons from π^0 decay cannot be separated from the process under study. The experimental data with special selection criteria are used to estimate this background. The procedure is similar to that used in the study of $e^+e^- \to \Lambda\bar{\Lambda}\pi^0$ background in Sec. III B. We selected two $\Sigma^0\bar{\Sigma}^0\pi^0$ candidates with an expected background from $e^+e^- \to \Lambda\bar{\Lambda}\gamma$ and $e^+e^- \to \Lambda\bar{\Sigma}^0\gamma$ processes of 0.5 ± 0.2 events. To suppress the $\Lambda\bar{\Sigma}^0\pi^0$ background in the $\Lambda\bar{\Sigma}^0\gamma$ sample we reject events with $0.10 < M_{2\gamma} < 0.17$ GeV/c^2, where $M_{2\gamma}$ is the invariant mass of the most energetic photon in an event and another photon with energy greater than 0.1 GeV. This removes about 1/3 of $\Lambda\bar{\Sigma}^0\pi^0$ events and less than 1% of signal events. After applying this selection criterion the rates at which $e^+e^- \to \Lambda\bar{\Sigma}^0\pi^0$ events are selected as $\Lambda\bar{\Sigma}^0\gamma$ or $\Lambda\bar{\Sigma}^0\pi^0$ are in the ratio (2.1 ± 0.2), and the $\Lambda\bar{\Sigma}^0\pi^0$ background in the $\Lambda\bar{\Sigma}^0\gamma$ event sample is estimated to be (3.1 ± 2.2) events. We assume that the dibaryon mass distribution for the $e^+e^- \to \Lambda\bar{\Sigma}^0\pi^0$ process is similar to that for the $e^+e^- \to p\bar{p}\pi^0$ process [1]. In particular, about 70% of the $e^+e^- \to \Lambda\bar{\Sigma}^0\pi^0$ events have $\Lambda\bar{\Sigma}^0$ mass less than 2.9 GeV/c^2. Both observed $\Lambda\bar{\Sigma}^0\pi^0$ events lie in this mass region.

The one-Σ^0 background other than $\Lambda\bar{\Sigma}^0\pi^0$ is estimated using the difference in the χ^2 distributions for signal and background events. Two histograms of $M_{\Lambda\gamma}$ for events with $\chi^2_{\Lambda\Sigma} < 20$ and with $20 < \chi^2_{\Lambda\Sigma} < 40$ are fitted simultaneously to the sum of the distributions for signal and background,

$$n_i = N_1 H_{1i} + N_2 H_{2i} + N_0 H_{0i}, \qquad (14)$$

where N_1, N_2, and N_0 are the numbers of events containing one, two, and zero Σ^0's in the final state, respectively. The one-Σ^0 events are the signal events with a possible contribution from the background processes $\Lambda\bar{\Sigma}^0\pi^0, \Lambda\bar{\Sigma}^0\pi^0\gamma$, etc. The function H_1 describing the mass distribution of one-Σ^0 events is calculated using $e^+e^- \to \Lambda\bar{\Sigma}^0\gamma$ simulation. The distribution of two-Σ^0 events is taken from $e^+e^- \to \Sigma^0\bar{\Sigma}^0\gamma$ simulation. The parameter N_2 is fixed by addition of the term $-\ln f_P(n_0; \mu_0)$ to minimize the likelihood function. Here f_P is a Poisson distribution, n_0 is the number of events in the two-Σ^0 sample described above, and $\mu_0 = \kappa r N_2$. The scale factor $\kappa = 0.80 \pm 0.05$ is found from $e^+e^- \to \Sigma^0\bar{\Sigma}^0\gamma$ simulation as the ratio of detection efficiencies for two-Σ^0 and $\Lambda\bar{\Sigma}^0\gamma$ selections. The factor $r \approx 1.1$ takes into account the purity of the two-Σ^0 sample, which is $(90 \pm 5)\%$. It should be noted

TABLE VIII. Comparison of the fit results for $\Lambda\bar{\Sigma}^0$ masses below 2.9 GeV/c^2 and the predictions from JETSET simulation; N_{1s}, N_0, N_{1b}, N_2, and $N_{\Lambda\bar{\Sigma}^0\pi^0}$ are the fitted numbers of signal, zero-, one-, two-Σ^0, and $\Sigma^0\bar{\Sigma}^0\pi^0$ background events with $\chi^2_{\Lambda\Sigma} < 20$, respectively.

	N_{1s}	N_2	N_0	N_{1b}	$N_{\Lambda\bar{\Sigma}^0\pi^0}$
Data	24.1 ± 8.4	13.8 ± 4.4	17.0 ± 7.8	<5	3.1 ± 2.2
JETSET	50 ± 6	17 ± 3	3.0 ± 1.5	0.6 ± 0.6	1.2 ± 0.9

that the two-Σ^0 sample contains not only $\Sigma^0\bar{\Sigma}^0\gamma$ but also events from the processes $e^+e^- \to \Sigma^0\bar{\Sigma}^0\pi^0$, $\Sigma^0\bar{\Sigma}^0\pi^0\gamma$, etc. A similar approach is used to introduce the $\Lambda\bar{\Sigma}^0\pi^0$ background into the fit. The shape of the zero-Σ^0 background (H_0) is modeled using the mass distribution for the $e^+e^- \to \Lambda\bar{\Lambda}\gamma$ process. The distribution is parametrized as $H_0 = (1 + a_0(M_{\Lambda\gamma} - m_\Sigma))f(M_\Sigma)$, where m_Σ is nominal Σ^0 mass. The function $f(M_{\Lambda\gamma})$ describes the deviation from a linear function due to our choice of one of the two $\Lambda(\bar{\Lambda})\gamma$ combinations. This function is equal to unity at the end points of the mass interval, and is about 2 at the center. We checked that the function H_0 with a_0 as a free parameter provides a good description of the mass
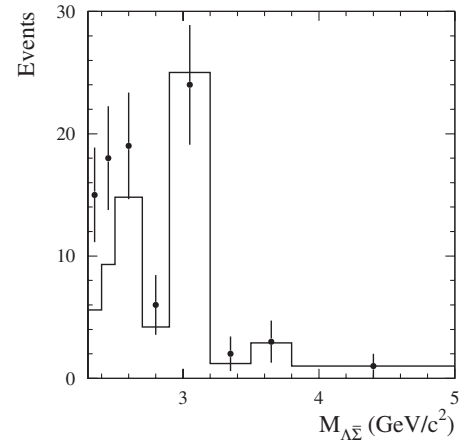

FIG. 30. The distribution of selected data events (points with error bars) over chosen mass intervals. The histogram shows fitted background.

TABLE IX. The values of the various efficiency corrections for the process $e^+e^- \to \Lambda\bar{\Sigma}^0\gamma$.

Effect	δ_i, (%)
$\chi^2_{\Lambda\Sigma} < 20$	-2.0 ± 6.0
Track reconstruction	-1.0 ± 3.8
$\bar{p}$ nuclear interaction	$+1.0 \pm 0.4$
PID	$+0.6 \pm 0.6$
Photon inefficiency	-2.6 ± 0.6
Photon conversion	$+0.8 \pm 0.4$
Total	-3.2 ± 7.2

TABLE X.   The $\Lambda\bar{\Sigma}^0$ invariant mass interval ($M_{\Lambda\bar{\Sigma}}$), net number of signal events (N_s), detection efficiency (ε), ISR luminosity (L), measured cross section (σ), and effective form factor (F) for $e^+e^- \to \Sigma^0\bar{\Sigma}^0$. The quoted errors on σ are statistical and systematic. For the form factor, the total error is listed.

$M_{\Lambda\bar{\Sigma}}$ (GeV/c^2)	N_s	ε	L (pb^{-1})	σ (pb)	$\|F\|$
2.308–2.400	$9.4^{+4.6}_{-4.1}$	0.035 ± 0.004	5.70	$47^{+23}_{-21} \pm 5$	$0.102^{+0.023}_{-0.027}$
2.400–2.500	$8.7^{+5.1}_{-4.7}$	0.041 ± 0.004	6.52	$32^{+19}_{-18} \pm 4$	$0.068^{+0.018}_{-0.022}$
2.500–2.700	$4.2^{+4.8}_{-4.4}$	0.042 ± 0.004	14.02	$7.1^{+8.2}_{-7.5} \pm 0.7$	$0.029^{+0.014}_{-0.029}$
2.700–2.900	$1.8^{+2.7}_{-2.3}$	0.041 ± 0.004	15.38	$2.9^{+4.3}_{-3.7} \pm 0.3$	$0.018^{+0.011}_{-0.018}$
2.900–3.300	<9.0	0.040 ± 0.004	25.78	<8.7	<0.033
3.300–3.500	<5.3	0.041 ± 0.005	29.28	<4.5	<0.025
3.500–3.800	<5.1	0.038 ± 0.005	33.13	<4.1	<0.026
3.800–5.000	<3.5	0.034 ± 0.004	180.38	<0.6	<0.011

distributions for simulated $e^+e^- \to \Lambda\bar{\Lambda}\pi^0$ and $e^+e^- \to \Lambda\bar{\Lambda}\pi^0\gamma$ events, and data $\Lambda\bar{\Lambda}\gamma$ events selected by requiring $\chi^2_{\Lambda\Lambda} < 20$ and $\chi^2_{\Lambda\Sigma} < 20$.

The one-Σ^0 background, other than that from $\Lambda\bar{\Sigma}^0\pi^0$, is estimated from the fit according to Eq. (6). The coefficients β_{sig} and β_{bkg} are obtained from the signal and $\Lambda\bar{\Sigma}^0\pi^0\gamma$ simulation and take the values 0.15 ± 0.02 and 1.5 ± 0.3, respectively. Their errors are enlarged to take into account the data-MC simulation difference in the χ^2 distributions resulting from the kinematic fits.

The fit results for $\Lambda\bar{\Sigma}^0$ masses below 2.9 GeV/c^2 are shown in Fig. 29 and summarized in Table VIII, together with the predictions from the JETSET simulation.

The fitting procedure was performed in eight $\Lambda\bar{\Sigma}^0$ mass intervals, and the resulting data distribution is compared to the fitted background in Fig. 30. An excess of signal events over background is seen only for $\Lambda\bar{\Sigma}^0$ masses below 2.9 GeV/c^2. The number of signal events in each mass interval is listed in Table X; 90% CL upper limits are given for the intervals with $M_\Lambda > 2.9$ GeV/c^2. The significance of the observation of $\Lambda\bar{\Sigma}^0$ production in the mass region below 2.9 GeV/c^2 is 3.3σ.

C. Cross section and form factor

The cross section for $e^+e^- \to \Lambda\bar{\Sigma}^0$ is calculated from the $\Lambda\bar{\Sigma}^0$ mass spectrum according to Eqs. (9) and (10).

The detection efficiency is determined from MC simulation and then corrected for data-MC simulation differences in detector response. The model dependence of the detection efficiency due to the unknown $|G_E/G_M|$ ratio is estimated to be 5%. The efficiency corrections summarized in Table IX were discussed in Secs. III D and IV C.

The corrected detection efficiencies are listed in Table X. The uncertainty in efficiency takes into account simulation statistical error, model uncertainty, the error on the $\Lambda \to p\pi^-$ branching fraction, and the uncertainty in the efficiency correction.

The measured values of the $e^+e^- \to \Lambda\bar{\Sigma}^0$ cross section are listed in Table X, together with those of the effective form factor.[3] The quoted cross section errors are statistical and systematic. The latter includes systematic uncertainty in detection efficiency, the error on the total integrated luminosity (1%), and the radiative-correction uncertainty (1%). This is the first measurement of the $e^+e^- \to \Lambda\bar{\Sigma}^0$ cross section. The upper limit set by DM2 [6] at 2.386 GeV (<75 pb) is consistent with our results.

Assuming that all events in the 2.90–3.30 GeV/c^2 mass range result from $J/\psi \to \Lambda\bar{\Sigma}^0$ decay, we obtain an upper limit for the $J/\psi \to \Lambda\bar{\Sigma}^0$ branching fraction $\mathcal{B}(J/\psi \to \Lambda\bar{\Sigma}^0) < 2 \times 10^{-4}$, which is slightly higher than the only other estimate, $\mathcal{B}(J/\psi \to \Lambda\bar{\Sigma}^0) < 1.5 \times 10^{-4}$ [26].

VI. SUMMARY

The processes $e^+e^- \to \Lambda\bar{\Lambda}\gamma$, $\Lambda\bar{\Sigma}^0\gamma$, and $\Sigma^0\bar{\Sigma}^0\gamma$ have been studied for dibaryon invariant mass up to 5 GeV/c^2. From the measured dibaryon mass spectra we obtained the $e^+e^- \to \Lambda\bar{\Lambda}$, $\Lambda\bar{\Sigma}^0$, and $\Sigma^0\bar{\Sigma}^0$ cross sections and baryon effective form factors. Our results on the measurements of the various baryon form factors for dibaryon invariant masses above $\Lambda\bar{\Lambda}$ threshold are shown in Fig. 31.

For $e^+e^- \to \Lambda\bar{\Lambda}\gamma$ we analyzed the Λ angular distributions in the mass range from threshold to 2.8 GeV/c^2 and extracted the $|G_E/G_M|$ ratio. Our results are

$$|G_E/G_M| = 1.73^{+0.99}_{-0.57} \quad \text{for 2.23–2.40 GeV/}c^2,$$

$$|G_E/G_M| = 0.71^{+0.66}_{-0.71} \quad \text{for 2.40–2.80 GeV/}c^2,$$

and are consistent both with $|G_E/G_M| = 1$ and with the results for $e^+e^- \to p\bar{p}$ [1], where this ratio was found to be significantly greater than unity near threshold.

---

[3]For the $e^+e^- \to \Lambda\bar{\Sigma}^0$ process, Eq. (3) must be modified by the substitutions $\beta = (1 - (m_\Lambda - m_\Sigma)^2/m^2)2P^*_\Lambda/m$ and $\tau = m^2/(m_\Lambda + m_\Sigma)^2$ [25], where P^*_Λ is the baryon momentum.
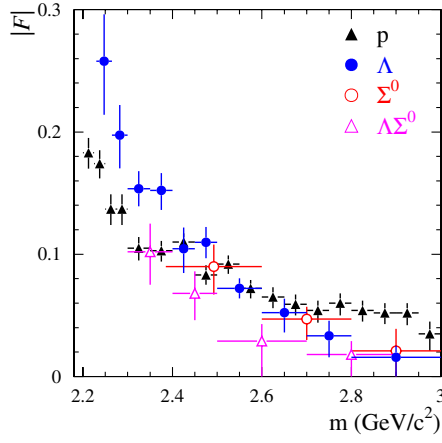
FIG. 31 (color online). The measured dependence of the baryon form factors on dibaryon invariant mass. The proton data are taken from Ref. [1].

The measurement of the Λ polarization enables the extraction of the relative phase between the Λ electric and magnetic form factors. The limited statistics of the present experiment allow us to set only very weak limits on this phase:

$$-0.76 < \sin\phi < 0.98.$$

From the events in the J/ψ and $\psi(2S)$ regions, the products

$$\Gamma(J/\psi \to e^+e^-)\mathcal{B}(J/\psi \to \Lambda\bar{\Lambda}) = (10.7 \pm 0.9 \pm 0.7)\,\text{eV},$$
$$\Gamma(J/\psi \to e^+e^-)\mathcal{B}(J/\psi \to \Sigma^0\bar{\Sigma}^0) = (6.4 \pm 1.2 \pm 0.6)\,\text{eV},$$
$$\Gamma(\psi(2S) \to e^+e^-)\mathcal{B}(\psi(2S) \to \Lambda\bar{\Lambda}) = (1.5 \pm 0.4 \pm 0.1)\,\text{eV}$$

have been measured, and, using the known e^+e^- partial widths, the corresponding branching ratios have been obtained:

$$\mathcal{B}(J/\psi \to \Lambda\bar{\Lambda}) = (1.92 \pm 0.21) \times 10^{-3},$$
$$\mathcal{B}(J/\psi \to \Sigma^0\bar{\Sigma}^0) = (1.16 \pm 0.26) \times 10^{-3},$$
$$\mathcal{B}(\psi(2S) \to \Lambda\bar{\Lambda}) = (6.0 \pm 1.5) \times 10^{-4}.$$

ACKNOWLEDGMENTS

APPENDIX: ANGULAR DISTRIBUTIONS AND Λ POLARIZATION IN THE $e^+e^- \to \Lambda\bar{\Lambda}\gamma$ REACTION

The formulas given in this section are taken from Ref. [3]. The process $e^+e^- \to \Lambda\bar{\Lambda}\gamma$ is considered in the e^+e^- center-of-mass frame, where the electron has momentum $\boldsymbol{p}$ and energy ε, and the photon has momentum $\boldsymbol{k}$ and energy ω. The Λ momentum $\boldsymbol{P}$ is given in the $\Lambda\bar{\Lambda}$ rest frame. The differential cross section summed over the polarization of one of the final particles is given by

$$d\sigma = \frac{\alpha^3 P d^3k d\Omega_\Lambda}{16\pi^2 \omega \varepsilon^2 Q[1 - (\mathbf{n} \cdot \boldsymbol{\nu})^2]} \mathcal{A}\left(1 + \boldsymbol{\zeta}_f \cdot \mathbf{s}\right),$$

$$\mathcal{A} = 2|G_M|^2(1 + N^2) + \left(\frac{4m_\Lambda^2}{Q^2}|G_E|^2 - |G_M|^2\right)$$
$$\times ([\mathbf{n} \times \mathbf{f}]^2 + [\mathbf{N} \times \mathbf{f}]^2),$$

$$\boldsymbol{\zeta}_f = \frac{4m_\Lambda}{Q\mathcal{A}} \text{Im}(G_E^* G_M)((\mathbf{n} \cdot \mathbf{f})[\mathbf{n} \times \mathbf{f}] + (\mathbf{N} \cdot \mathbf{f})[\mathbf{N} \times \mathbf{f}]);$$

$$\mathbf{n} = \frac{\mathbf{k}}{\omega},$$

$$\boldsymbol{\nu} = \frac{\mathbf{p}}{\varepsilon},$$

$$\mathbf{N} = \frac{\boldsymbol{\nu} + (\gamma - 1)(\mathbf{n} \cdot \boldsymbol{\nu})\mathbf{n}}{\sqrt{\gamma^2 - 1}},$$

$$N^2 = (\mathbf{n} \cdot \boldsymbol{\nu})^2 + \frac{1}{\gamma^2 - 1},$$

$$\gamma = \frac{2\varepsilon - \omega}{Q},$$

$$Q = \sqrt{\varepsilon(\varepsilon - \omega)},$$

$$P = |\mathbf{P}| = \sqrt{Q^2/4 - m_\Lambda^2},$$

$$\mathbf{f} = \frac{\mathbf{P}}{P}.$$

Here $\mathbf{s}$ and $\boldsymbol{\zeta}_f$ are the spin and polarization vectors of the Λ in its rest frame.

[1] B. Aubert *et al.* (*BABAR* Collaboration), Phys. Rev. D **73**, 012005 (2006).

[2] G. Bonneau and F. Martin, Nucl. Phys. **B27**, 381 (1971).

[3] L. V. Kardapoltzev, Bachelor's thesis, Novosibirsk State University, 2007 (unpublished).

[4] A. Z. Dubnickova, S. Dubnicka, and M. P. Rekalo, Nuovo Cimento Soc. Ital. Fis. A **109**, 241 (1996).

[5] H. Czyz, A. Grzelinska, and J. H. Kuhn, Phys. Rev. D **75**, 074026 (2007).

[6] D. Bisello *et al.* (DM2 Collaboration), Z. Phys. C **48**, 23 (1990).

[7] B. Aubert *et al.* (*BABAR* Collaboration), Nucl. Instrum. Methods Phys. Res., Sect. A **479**, 1 (2002).

[8] G. Rodrigo *et al.*, Eur. Phys. J. C **24**, 71 (2002).

[9] H. Czyz *et al.*, Eur. Phys. J. C **35**, 527 (2004).

[10] S. Agostinelli *et al.* (GEANT4 Collaboration), Nucl. Instrum. Methods Phys. Res., Sect. A **506**, 250 (2003).

[11] T. Sjöstrand, Comput. Phys. Commun. **82**, 74 (1994).

[12] M. Caffo, H. Czyz, and E. Remiddi, Nuovo Cimento Soc. Ital. Fis. A **110**, 515 (1997); Phys. Lett. B **327**, 369 (1994).

[13] W.-M. Yao *et al.* (Particle Data Group), J. Phys. G **33**, 1 (2006).

[14] M. W. Eaton *et al.* (MARKII Collaboration), Phys. Rev. D **29**, 804 (1984).

[15] D. Pallin *et al.* (DM2 Collaboration), Nucl. Phys. **B292**, 653 (1987).

[16] M. Ablikim *et al.* (BES Collaboration), Phys. Lett. B **632**, 181 (2006).

[17] J. Haidenbauer, H. W. Hammer, U. G. Meissner, and A. Sibirtsev, Phys. Lett. B **643**, 29 (2006).

[18] V. F. Dmitriev and A. I. Milstein, Nucl. Phys. B, Proc. Suppl. **162**, 53 (2006).

[19] B. Aubert *et al.* (*BABAR* Collaboration), Phys. Rev. D **71**, 052001 (2005).

[20] M. Benayoun *et al.*, Mod. Phys. Lett. A **14**, 2605 (1999).

[21] C. Carimalo, Int. J. Mod. Phys. A **2**, 249 (1987).

[22] T. K. Pedlar *et al.* (CLEO Collaboration), Phys. Rev. D **72**, 051108 (2005).

[23] M. Ablikim *et al.* (BES Collaboration), Phys. Lett. B **648**, 149 (2007).

[24] B. Aubert *et al.* (*BABAR* Collaboration), Phys. Rev. D **73**, 052003 (2006).

[25] A. I. Milstein (private communication).

[26] I. Peruzzi *et al.* (MARKI Collaboration), Phys. Rev. D **17**, 2901 (1978).